

Note: As near as I can tell, this is a recreation
from my sources of the paper that appeared in:

Wells WM, Kikinis R, Grimson WEL, Jolesz F.
Adaptive segmentation of MRI data.
IEEE Transactions on Medical Imaging. 1996;15:429--442.

Warning: the version that was printed by the IEEE contains errors in
some of the equations that were introduced by the IEEE "typesetters".

Mar 21, 2000, sw

Adaptive Segmentation of MRI data

W. M. Wells III ^{*} W.E.L. Grimson [†] R. Kikinis [‡] F. A. Jolesz [§]

Abstract

Intensity-based classification of MR images has proven problematic, even when advanced techniques are used. Intra-scan and inter-scan intensity inhomogeneities are a common source of difficulty. While reported methods have had some success in correcting intra-scan inhomogeneities, such methods require supervision for the individual scan. This paper describes a new method called *adaptive segmentation* that uses knowledge of tissue intensity properties and intensity inhomogeneities to correct and segment MR images. Use of the EM algorithm leads to a method that allows for more accurate segmentation of tissue types as well as better visualization of MRI data, that has proven to be effective in a study that includes more than 1000 brain scans.

Implementation and results are described for segmenting the brain in the following types of images: axial (dual-echo spin-echo), coronal (3DFT gradient-echo T1-weighted) all using a conventional head coil; and a sagittal section acquired using a surface coil.

The accuracy of adaptive segmentation was found to be comparable with manual segmentation, and closer to manual segmentation than supervised multi-variate classification while segmenting gray and white matter.

Keywords:

- Magnetic Resonance Imaging
- Segmentation
- Intensity Inhomogeneity
- Expectation-Maximization Algorithm

^{*}Harvard Medical School and Brigham and Women's Hospital, Department of Radiology, 75 Francis St., Boston, MA 02115, sw@ai.mit.edu

[†]Massachusetts Institute of Technology, Artificial Intelligence Laboratory, 545 Technology Square, Cambridge, MA 02139, welg@ai.mit.edu

[‡]Harvard Medical School and Brigham and Women's Hospital, Department of Radiology, 75 Francis St., Boston, MA 02115, kikinis@bwh.harvard.edu

[§]Harvard Medical School and Brigham and Women's Hospital, Department of Radiology, 75 Francis St., Boston, MA 02115, jolesz@bwh.harvard.edu

1 Introduction

The advantages of magnetic resonance imaging (MRI) over other diagnostic imaging modalities are its high spatial resolution and excellent discrimination of soft tissues. MRI provides rich information about anatomical structure, enabling quantitative pathological or clinical studies [1]; the derivation of computerized anatomical atlases [2]; as well as pre- and intra-operative guidance for therapeutic intervention [3, 4]. Such information is also valuable as an anatomical reference for functional modalities, such as PET [5], SPECT, and functional MRI [6].

Advanced applications that use the morphologic contents of MRI frequently require segmentation of the imaged volume into tissue types. This problem has received considerable attention – the comprehensive survey article by Bezdek et al. [7] lists 90 citations.

Such tissue segmentation is often achieved by applying statistical classification methods to the signal intensities [8, 9], in conjunction with morphological image processing operations [10, 11].

Conventional intensity-based classification of MR images has proven problematic, however, even when advanced techniques such as non-parametric, multi-channel methods are used. Intra-scan intensity inhomogeneities due to RF coils or acquisition sequences (e.g. susceptibility artifacts in gradient echo images) are a common source of difficulty. Although MRI images may appear visually uniform, such intra-scan inhomogeneities often disturb intensity-based segmentation methods. In the ideal case, differentiation between white and gray matter in the brain should be easy since these tissue types exhibit distinct signal intensities. In practice, spatial intensity inhomogeneities are often of sufficient magnitude to cause the distributions of signal intensities associated with these tissue classes to overlap significantly. In addition, the operating conditions and status of the MR equipment frequently affect the observed intensities, causing significant inter-scan intensity inhomogeneities that often necessitate manual training on a per-scan basis.

While reported methods [12, 13, 14, 15, 16, 17] have had some success in correcting intra-scan inhomogeneities, such methods require supervision for the individual scan. It was our goal to develop a fully automated segmentation algorithm for MR data that can handle the intra-scan and inter-scan intensity inhomogeneities that frequently arise.

This paper describes a new method called *adaptive segmentation* that uses knowledge of tissue properties and intensity inhomogeneities to correct and segment MR images. Use of the expectation-maximization algorithm leads to a method that allows for more accurate segmentation of tissue types as well as better visualization of MRI data. Adaptive segmentation has proven to be an effective fully-automatic means of segmenting brain tissue in a study including more than 1000 brain scans.

The method is described in Section 2, and a selection of segmentation results are presented in Section 3. A comparison of the method to manual and supervised segmentation

is described in Section 4, and the relation of adaptive segmentation to other methods is discussed in Section 5. Finally, some conclusions are drawn in Section 6.

2 Description of Method

We model intra- and inter-scan MRI intensity inhomogeneities with a spatially-varying factor called the *gain field* that multiplies the intensity data. The application of a logarithmic transformation to the intensities allows the artifact to be modeled as an additive *bias field*.

If the gain field is known, then it is relatively easy to estimate tissue class by applying a conventional intensity-based segmenter to the corrected data. Similarly, if the tissue classes are known, then it is straightforward to estimate the gain field by comparing predicted intensities and observed intensities. It may be problematic, however, to determine either the gain or the tissue type without knowledge of the other. We will show, however, that is possible to estimate both using an iterative algorithm (that converges in five to ten iterations, typically).

2.1 Bias Field Estimator

We use a Bayesian approach to estimating the bias field that represents the gain artifact in log-transformed MR intensity data. We first compute a logarithmic transformation of the intensity data as follows,

$$Y_i = g(X_i) = (\ln([X_i]_1), \ln([X_i]_2), \dots, \ln([X_i]_m))^T, \quad (1)$$

where X_i is the observed MRI signal intensity at the i -th voxel, and m is the dimension of the MRI signal.¹

Similar to other statistical approaches to intensity-based segmentation of MRI [10, 11], the distribution for observed values is modeled as a normal distribution (with the incorporation of an explicit bias field):

$$p(Y_i | \Gamma_i, \beta_i) = G_{\psi_{\Gamma_i}}(Y_i - \mu(\Gamma_i) - \beta_i), \quad (2)$$

where

$$G_{\psi_{\Gamma_i}}(x) \equiv (2\pi)^{-\frac{m}{2}} |\psi_{\Gamma_i}|^{-\frac{1}{2}} \exp\left(-\frac{1}{2} x^T \psi_{\Gamma_i}^{-1} x\right)$$

is the m -dimensional Gaussian distribution with variance ψ_{Γ_i} , and where

¹For example, m will be two for a double-echo MRI acquisition.

Y_i is the observed log-transformed intensities at the i^{th} voxel
 Γ_i is the tissue class at the i^{th} voxel²
 $\mu(x)$ is the mean intensity for tissue class x
 ψ_x is the covariance matrix for tissue class x
 β_i is the bias field at the i^{th} voxel.

Here Y_i , $\mu(x)$, and β_i are represented by m -dimensional column vectors, while ψ_x is represented by an m -by- m matrix. Note that the bias field has a separate value for each component of the log-intensity signal at each voxel. In words, Equation 2 states that the probability of observing a particular image intensity, given knowledge of the tissue class and the bias field is given by a Gaussian distribution centered at the biased mean intensity for the class.

A stationary prior (before the image data is seen) probability distribution on tissue class is used, it is denoted

$$p(\Gamma_i) . \quad (3)$$

If this probability is uniform over tissue classes, our method devolves to a maximum-likelihood approach to the tissue classification component. A spatially-varying prior probability density on brain tissue class is described in [18]. Such a model might profitably be used within this framework.

The entire bias field is denoted by $\beta = (\beta_0, \beta_1, \dots, \beta_{n-1})^T$, where n is the number of voxels of data. The bias field is modeled by a n -dimensional zero mean Gaussian prior probability density. This model allows us to capture the smoothness that is apparent in these inhomogeneities:

$$p(\beta) = G_{\psi_\beta}(\beta) , \quad (4)$$

where

$$G_{\psi_\beta}(x) \equiv (2\pi)^{-\frac{n}{2}} |\psi_\beta|^{-\frac{1}{2}} \exp\left(-\frac{1}{2} x^T \psi_\beta^{-1} x\right)$$

is the n -dimensional Gaussian distribution. The $n \times n$ covariance matrix for the entire bias field is denoted ψ_β . Although ψ_β will be too large to manipulate directly in practice, we will show below that tractable estimators result when ψ_β is chosen so that it is banded.

We assume that the bias field and the tissue classes are statistically independent, this follows if the intensity inhomogeneities originate in the equipment. Using the definition of conditional probability we may obtain the joint probability on intensity and tissue class conditioned on the bias field as follows,

$$p(Y_i, \Gamma_i | \beta_i) = p(Y_i | \Gamma_i, \beta_i) p(\Gamma_i) , \quad (5)$$

and we may obtain the conditional probability of intensity alone by computing a marginal

²For example, when segmenting brain tissue $\Gamma_i \in \{\textit{white matter}, \textit{gray matter}, \textit{cerebro-spinal fluid}\}$.

over tissue class:

$$p(Y_i | \beta_i) = \sum_{\Gamma_i} p(Y_i, \Gamma_i | \beta_i) = \sum_{\Gamma_i} p(Y_i | \Gamma_i, \beta_i) p(\Gamma_i) . \quad (6)$$

Thus, our modeling has led to a class-independent intensity distribution that is a mixture of Gaussian populations (one population for each tissue class). Since this model is a Gaussian mixture, rather than a purely Gaussian distribution, the estimators that we derive below will be non-linear.

We assume statistical independence of the voxel intensities (in other words, the noise in the MR signal is spatially white). We may then write the probability density for the entire image as

$$p(Y | \beta) = \prod_i p(Y_i | \beta_i) . \quad (7)$$

Bayes' rule may then be used to obtain the posterior probability of the bias field, given observed intensity data as follows,

$$p(\beta | Y) = \frac{p(Y | \beta) p(\beta)}{p(Y)} , \quad (8)$$

where $p(Y)$ is an unimportant normalizing constant.

Having obtained the posterior probability on the bias field, we now use the maximum-a-posteriori (MAP) principle to formulate an estimate of the bias field as the value of β having the largest posterior probability,

$$\hat{\beta} = \arg \max_{\beta} p(\beta | Y) . \quad (9)$$

A necessary condition for a maximum of the posterior probability of β is that its gradient with respect to β be zero. We use an equivalent zero-gradient condition on the logarithm of the posterior probability,

$$\left[\frac{\partial}{\partial [\beta_i]_k} \ln p(\beta | Y) \right]_{\beta=\hat{\beta}} = 0 \quad \forall_{i,k} , \quad (10)$$

where $[\beta_i]_k$ is the k -th component of the bias field at voxel i . Installing the statistical modeling of Equations 2-9 yields the following expression for the zero gradient condition:

$$\left[\frac{\partial}{\partial [\beta_i]_k} \left(\sum_j \ln p(Y_j | \beta_j) + \ln p(\beta) \right) \right]_{\beta=\hat{\beta}} = 0 \quad \forall_{i,k} .$$

Since only the i -th term of the sum depends on β_i , we have (after differentiating the logarithms)

$$\left[\frac{\frac{\partial}{\partial [\beta_i]_k} p(Y_i | \beta_i)}{p(Y_i | \beta_i)} + \frac{\frac{\partial}{\partial [\beta_i]_k} p(\beta)}{p(\beta)} \right]_{\beta=\hat{\beta}} = 0 \quad \forall_{i,k} .$$

Using Equations 2 and 6, this may be re-written as

$$\left[\frac{\sum_{\Gamma_i} p(\Gamma_i) \frac{\partial}{\partial [\beta_{i,k}]} G_{\psi_{\Gamma_i}}(Y_i - \mu(\Gamma_i) - \beta_i)}{\sum_{\Gamma_i} p(\Gamma_i) G_{\psi_{\Gamma_i}}(Y_i - \mu(\Gamma_i) - \beta_i)} + \frac{\frac{\partial}{\partial [\beta_{i,k}]} p(\beta)}{p(\beta)} \right]_{\beta=\hat{\beta}} = 0 \quad \forall_{i,k} .$$

Differentiating the Gaussian expression in the first term yields

$$\left[\frac{\sum_{\Gamma_i} p(\Gamma_i) G_{\psi_{\Gamma_i}}(Y_i - \mu(\Gamma_i) - \beta_i) \left[\psi_{\Gamma_i}^{-1}(Y_i - \mu(\Gamma_i) - \beta_i) \right]_k}{\sum_{\Gamma_i} p(\Gamma_i) G_{\psi_{\Gamma_i}}(Y_i - \mu(\Gamma_i) - \beta_i)} + \frac{\frac{\partial}{\partial [\beta_{i,k}]} p(\beta)}{p(\beta)} \right]_{\beta=\hat{\beta}} = 0 \quad \forall_{i,k} .$$

This expression may be written more compactly as

$$\left[\sum_j W_{ij} \left[\psi_j^{-1}(Y_i - \mu_j - \beta_i) \right]_k + \frac{\frac{\partial}{\partial [\beta_{i,k}]} p(\beta)}{p(\beta)} \right]_{\beta=\hat{\beta}} = 0 \quad \forall_{i,k} , \quad (11)$$

with the following definition of W_{ij} , (which are called the *weights*),

$$W_{ij} \equiv \frac{\left[p(\Gamma_i) G_{\psi_{\Gamma_i}}(Y_i - \mu(\Gamma_i) - \beta_i) \right]_{\Gamma_i=\text{tissue-class-}j}}{\sum_{\Gamma_i} p(\Gamma_i) G_{\psi_{\Gamma_i}}(Y_i - \mu(\Gamma_i) - \beta_i)} , \quad (12)$$

where subscripts i and j refer to voxel index and tissue class respectively, and defining

$$\mu_j \equiv \mu(\text{tissue-class-}j)$$

as the mean intensity of tissue class j . Equation 11 may be re-expressed as follows,

$$\left[\sum_j W_{ij} \left[\psi_j^{-1}(Y_i - \mu_j) \right]_k - \sum_j W_{ij} \left[\psi_j^{-1} \beta_i \right]_k + \frac{\frac{\partial}{\partial [\beta_{i,k}]} p(\beta)}{p(\beta)} \right]_{\beta=\hat{\beta}} = 0 \quad \forall_{i,k} ,$$

or as

$$\left[\left[\bar{R}_i \right]_k - \left[\overline{\psi^{-1}}_{ii} \beta_i \right]_k + \frac{\frac{\partial}{\partial [\beta_{i,k}]} p(\beta)}{p(\beta)} \right]_{\beta=\hat{\beta}} = 0 \quad \forall_{i,k} \quad (13)$$

with the following definitions for the mean residual,

$$\bar{R}_i \equiv \sum_j W_{ij} \psi_j^{-1}(Y_i - \mu_j) , \quad (14)$$

and the mean inverse covariance,

$$\overline{\psi^{-1}}_{ik} \equiv \begin{cases} \sum_j W_{ij} \psi_j^{-1} & \text{if } i = k \\ 0 & \text{otherwise} \end{cases} . \quad (15)$$

The mean residuals and mean inverse covariances defined above are averages taken over the tissue classes, weighted according to W_{ij} .

Equation 13 may be re-expressed in matrix notation as

$$\left[\overline{R} - \overline{\psi^{-1}}\beta + \frac{\nabla_{\beta} p(\beta)}{p(\beta)} \right]_{\beta=\hat{\beta}} = \mathbf{0} .$$

Differentiating the last term yields the following,

$$\overline{R} - \overline{\psi^{-1}}\hat{\beta} - \psi_{\beta}^{-1}\hat{\beta} = \mathbf{0} .$$

Finally, the zero-gradient condition for the bias field estimator may be written concisely as

$$\hat{\beta} = H\overline{R} , \quad (16)$$

where the linear operator H is defined by

$$H \equiv \left[\overline{\psi^{-1}} + \psi_{\beta}^{-1} \right]^{-1} , \quad (17)$$

that is, the bias field estimate is derived by applying the linear operator H to the mean residual field, and H is determined by the mean covariance of the tissue class intensities and the covariance of the bias field.

The bias field estimator of Equation 16 has some resemblance to being a linear estimator in Y of the bias field β . It is not a linear estimator, however, owing to the fact that the W_{ij} (the “weights”) that appear in the expression for \overline{R} and H are themselves non-linear functions of Y (Equation 12).

The result of the statistical modeling in this section has been to formulate the problem of estimating the bias field as a non-linear optimization problem embodied in Equation 16. This optimization depends on the mean residual of observed intensities and the mean intensity of each tissue class, and on the mean covariance of the tissue class intensities and the covariance of the bias field. In the next section an approach to obtaining solutions (estimates) is described.

2.2 EM Algorithm

We use the expectation-maximization (EM) algorithm to obtain bias field estimates from the non-linear estimator of Equation 16. The EM algorithm was originally described in its general form by Dempster, Laird and Rubin [19]. It is often used in estimation problems where some of the data are “missing.” In this application, the missing data is knowledge of the tissue classes. (If they were known, then estimating the bias field would be straightforward.)

In this application, the EM algorithm iteratively alternates evaluations of the expressions appearing in Equations 16 and 12,

$$W_{ij} \leftarrow \frac{\left[p(\Gamma_i) G_{\psi_{\Gamma_i}}(Y_i - \mu(\Gamma_i) - \beta_i) \right]_{\Gamma_i = \text{tissue-class-}j}}{\sum_{\Gamma_i} p(\Gamma_i) G_{\psi_{\Gamma_i}}(Y_i - \mu(\Gamma_i) - \beta_i)} , \quad (18)$$

$$\hat{\beta} \leftarrow H\bar{R} . \quad (19)$$

In other words, Equation 12 is used to estimate the weights given an estimated bias field, then Equation 19 is used to estimate the bias, given estimates of the weights.

As frequently occurs in application of the EM algorithm, the two components of the iteration have simple interpretations. Equation 18 (the *E-Step*) is equivalent to calculating the posterior tissue class probabilities (a good indicator of tissue class) when the bias field is known. Equation 19 (the *M-Step*) is equivalent to a MAP estimator of the bias field when the tissue probabilities W are known.

The iteration may be started on either expression. Initial values for the weights will be needed to start with Equation 19, and initial values for the bias field will be needed to start with Equation 18.

It is shown in [19] that in many cases the EM algorithm enjoys pleasant convergence properties – namely that iterations will never worsen the value of the objective function. Provided that the bias estimates are bounded, our model satisfies the necessary conditions for guaranteed convergence (although there is no guarantee of convergence to the global minimum).

In principle, given $\mu(\Gamma_i)$, ψ_β , and ψ_j , we could use the EM algorithm to obtain the needed estimates. In practice, we cannot directly measure ψ_β , and thus we will seek other estimates of ψ_β (in Section 2.3).

2.2.1 Tractability of the M Step

Although the covariance matrix ψ_β that characterizes the prior on bias fields is impractically large in general, we will demonstrate that tractable estimation algorithms may yet be obtained.

From an engineering standpoint, ψ_β may be chosen in the following way,

$$\psi_\beta = LL^T \quad (20)$$

where L represents a “practical” low-pass filter. Then (referring to Equation 4)

$$p(\beta) \propto \exp\left(-\frac{1}{2} |L^{-1}\beta|^2\right) ,$$

and L^{-1} will amplify high-frequency components of β since it is the inverse of a low-pass filter. It is clear that this form of prior model on bias fields will have lower probabilities to the extent that the bias field contains high-frequency components.

Further, ψ_β may be chosen to be a banded matrix, this will occur if L represents a FIR (finite impulse-response) low-pass filter. Equation 16 may be written in the following way

$$\left[I + \psi_\beta \overline{\psi^{-1}} \right] \hat{\beta} = \psi_\beta \bar{R} .$$

In this case, calculating $\psi_\beta \overline{R}$ is tractable, since ψ_β is banded, and solving the linear system for $\hat{\beta}$ will also be tractable, since $[I + \psi_\beta \overline{\psi^{-1}}]$ is banded (note that $\overline{\psi^{-1}}$ is diagonal).

2.3 Determination of the Linear Operator H

In this section we discuss the linear operator H , including its relation to the prior model on bias fields. We argue that H will be a linear low-pass filter, and describe a particularly efficient filter.

2.3.1 Discussion

We have taken a Bayesian approach to estimating the bias field and tissue classes, and a formal prior model on bias fields has been assumed. This approach has allowed us to derive a version of the EM algorithm for this application. The operator H is related to the prior on the bias field via ψ_β^{-1} and to the measurement noise via $\overline{\psi^{-1}}$ (Equation 17). Ideally, H would be determined by estimating the covariance ψ_β , but given the size of this matrix, such an approach is impractical.

As pointed out above, H is the MAP estimator of the bias field when the tissue probabilities are known, (the “complete-data” case with the EM algorithm). As such, H is an optimal estimator (with respect to the Gaussian modeling), and is also the optimal *linear* least squares estimator (LLSE) for arbitrary zero-mean models of the bias field whose second-order statistics are characterized by ψ_β .

Optimal filters may often be equivalently characterized within the related formalisms of estimation theory and random processes. Although filters are perhaps more commonly described within the framework of random processes, we have used estimation theory in order to derive the EM algorithm for this application. H is essentially equivalent to the LLSE for discrete random processes with given second order statistics (auto-correlation functions). Such estimators are characterized by the Wiener-Hopf equations. Applications of Wiener filtering are often approached via Fourier transform methods, yielding a filter frequency response in terms of the power spectra of the signal and noise. In such applications, the noise spectra are often known, and the signal spectra are sometimes estimated using techniques of spectral estimation.

A frequent problem that arises in filter design (the present complete-data case included) is that of estimating a slowly-varying signal that has been contaminated with white noise. The optimal filter in such situations will be a low-pass filter [20, Section 9.2].

In practice, it is difficult to obtain *the* optimal linear filter. H may be instead chosen as a good engineering approximation of the optimal linear filter (this approach is described in more detail below). In this case, Equations 18 and 19 are still a useful estimator for the missing data case, and the good convergence properties of the EM algorithm still apply.

This is the approach we have taken in our implementations, where the filter was selected empirically.

Examination of the bias fields displayed in Figures 6 and 11 shows that they are slowly varying. While the low-pass filters H we have used in practice are not the optimal filters for estimating these bias fields, they are reasonable choices, and may correspond to reasonable subjective estimates of the unknown probability law for bias fields, in the sense described by Friden [21, Chapter 16]. In the end, they are justified empirically by the good results obtained via their use. Because ψ_β is required to be positive definite, not all choices of low-pass filter H will correspond to formally valid prior models on the bias field.

2.3.2 Computationally Efficient Filter

As argued above, the optimal H will be a linear low-pass filter, when tissue class is constant. We have employed a particularly efficient filter that is characterized as follows

$$\hat{\beta}_i = \frac{[F\overline{R}]_i}{[F\overline{\psi^{-1}}\mathbf{1}]_i} \quad (21)$$

where

$$\mathbf{1} \equiv (1, 1, 1, \dots, 1)^T .$$

The filter specified above is clearly linear in the mean residual, and it will be a low-pass filter when the tissue class is constant, provided that F is a low-pass filter. It has been designed to have unity DC gain – a spatially constant shift in Y induces the same constant shift in $\hat{\beta}$. If F is chosen to be a computationally efficient low-pass filter, then the filter specified by Equation 21 will also be computationally efficient.

2.4 Equal Covariance Case

The formalism simplifies somewhat when the tissue classes have the same covariance. In this case, $\psi_j^{-1} = \psi^{-1}$ and

$$\overline{\psi^{-1}}_{ii} = \sum_j W_{ij} \psi^{-1} = \psi^{-1}$$

so that

$$\overline{\psi^{-1}} = \text{DIAG}(\psi^{-1}, \psi^{-1}, \psi^{-1}, \dots, \psi^{-1}) .$$

In this case H will be essentially a shift-invariant linear filter, provided that the bias model is stationary. The expression for the mean residual simplifies to the following matrix expression

$$\overline{R} = \overline{\psi^{-1}}[Y - WU]$$

where W is the matrix of the weights W_{ij} , and U is a column vector containing the class mean intensities $U \equiv (\mu_1, \mu_2, \dots, \mu_m)^T$.

In the case of scalar data, $\psi^{-1} = \frac{1}{\sigma^2}$, and the bias estimator may be written as

$$\hat{\beta} = [I + \sigma^2 \psi_\beta^{-1}]^{-1} [Y - WU] . \quad (22)$$

This expression for the bias estimator was previously reported in [22], along with scalar formulas for the weights. The bias estimator of Equation 22 is particularly simple when the bias model is stationary. It is a shift-invariant linear low-pass filter applied to the difference between the observed intensities and a prediction of the signal that is based on the weights (which are a good estimator of tissue class).

2.5 Non-Parametric Generalization

This section describes an extension of the segmentation method that uses a form of non-parametric tissue class conditional intensity models that are described in [23]. The motivation was to bring the benefits of intensity inhomogeneity correction to applications that were currently being processed in the manner of [23].

The method that was described in previous sections has two main components: tissue classification and bias field estimation. Our approach in the extended method has been to use the same basic iteration, and to replace the tissue classification component with the technique described in [23]. In more detail, we use the intensity probability densities described in [23] for the calculation of the weights in the E step, and substitute approximations of the means and covariances of the non-parametric densities for the means and covariances that appear in Equations 14 and 15.

The classifier described in [23] uses the *Parzen Window* representation for non-parametric probability densities [24] that are derived from training data . The tissue class conditional models may be written as follows,

$$p_X(X_i | \Gamma_i = \text{tissue-class-}j) = \frac{1}{n_j} \sum_k G_{\psi_0}(X_i - X_{kj}) , \quad (23)$$

where X_i is the MR intensity at voxel i , $G_{\psi_0}(x)$ is a radially-symmetric Gaussian density, and X_{kj} are the intensities of the n_j training points for tissue class j .

The non-parametric tissue class conditional intensity models are derived from training in the “natural” MR intensities. In view of our logarithmic transformation of the intensity data (Equation 1), we use the following standard formula for transforming probability densities,

$$p_Y(Y_i | \Gamma_i) = \frac{p_X(g^{-1}(Y_i) | \Gamma_i)}{\left| \frac{\partial g}{\partial X_i} \right| | g^{-1}(Y_i) |} .$$

For double-echo data the resulting expression for the probability density on log-transformed data is

$$p_Y(Y_i | \Gamma_i) = \exp(Y_1) \exp(Y_2) p_X((\exp(Y_1), \exp(Y_2))^T | \Gamma_i) ,$$

where p_X is the non-parametric density described in Equation 23.

In the expression for the weights (Equation 18), we use the non-parametric class conditional densities $p_Y(Y_i - \beta_i | \Gamma_i)$ in place of the Gaussian densities $G_{\psi_{\Gamma_i}}(Y_i - \mu(\Gamma_i) - \beta_i)$.

In the expressions for the average residual (Equation 14) and average covariance (Equation 15) we approximate with the empirical tissue class means and covariances from the log transformed training data, as follows,

$$\mu_j = \frac{1}{n_j} \sum_k Y_{kj}$$

and

$$\psi_j = \frac{1}{n_j} \sum_k (Y_{kj} - \mu_j)(Y_{kj} - \mu_j)^T ,$$

where $Y_{kj} = g(X_{kj})$ are the n_j log-transformed intensities of the training points for tissue class j .

The resulting iterative algorithm is a simple generalization from the Gaussian theory developed in the previous sections. This method was designed to be a compatible replacement for an existing method [23] that did not address the issue of intensity inhomogeneities. While the extended method is not technically an instance of the EM algorithm, it has proven to be robust in practice. Results obtained using the method are described in Section 3.2.

2.6 Implementations

2.6.1 Single-Channel Implementation

The single-channel results described in Section 3.1 were obtained using an implementation of the adaptive segmentation method as described in Section 2.4, that was coded in the C programming language. This single-channel, 2D implementation accommodates two tissue classes, and uses a pre-defined region of interest (ROI) to limit the part of the image to be classified and gain-corrected.

The algorithm of Section 2.2 has been initiated on the ‘‘E step’’, Equation 18, with a flat initial bias field, and on the ‘‘M step’’, Equation 19, with equal tissue class probabilities.

Iterated moving-average low-pass filters [25] have been used for the operator H in Equation 19. These filters have a low computational cost that is independent of the width of their support (amount of smoothing). The filters have been adapted to only operate in the ROI, and to adjust the effective averaging window at boundaries to confine influence to the ROI. These filters are shift-invariant, except at the boundary regions. Averaging window widths of 11 – 30 pixels were used. One to four filtering passes have been used with similar results. Usually, one pass is used for the sake of efficiency. A uniform distribution was used for the prior on tissue class.

In a typical case, the program was run until the estimates stabilized, typically in 5 – 10 iterations, requiring approximately .5 second per iteration (per 256^2 slice) on a Sun Microsystems Sparcstation 10 [26].

2.6.2 Two-Channel Implementation

The double-echo results described in Section 3.2 were obtained using an implementation of the non-parametric extension that is described in Section 2.5. This implementation is also coded in the C programming language. It accommodates 2 channel data (typically registered proton-density and T2-weighted images), and multiple (more than two) tissue classes having un-equal covariances. Because it can model the important intensities in the imagery (including the background signal) it is able to correct and segment brain images without the need for a previously generated ROI. It uses the computationally-efficient filter described in Section 2.3.2, F is implemented as a moving average filter. Both uniform and non-uniform distributions have been used for the prior on tissue class.

In a typical case, the program was run until the estimates stabilized, typically in 5 – 10 iterations, requiring approximately 2 seconds per iteration (per 256^2 slice pair) on a Sun Microsystems Sparcstation 10 [26].

3 Results

In this section we describe the application of adaptive segmentation to segmentation of the human brain from spin-echo and gradient-echo images. Examples are shown for the following types of brain images: axial (dual-echo spin-echo), coronal (3DFT gradient-echo T1-weighted) all using a conventional head coil; and a sagittal section acquired using a surface coil. An additional example is shown for a synthetic image.

All of the MR images shown in this section were obtained using a General Electric Signa 1.5 Tesla clinical MR imager [27]. An anisotropic diffusion filter developed by Gerig et al. [28] was used as a pre-processing step to reduce noise.

The method has been found to be substantially insensitive to parameter settings. For a given type of acquisition, intensity variations across patients, scans, and equipment changes have been accommodated in the estimated bias fields without the need for manual intervention. In this sense, the method is fully automatic for segmenting healthy brain tissue.

3.1 Single-Channel Examples

This section shows a selection of results obtained using the single-channel implementation that is described in Sections 2.4 and 2.6.1. Operating parameters (tissue model parameters

and filter parameters) were selected manually.

3.1.1 Synthetic Example

Figure 1 shows a synthetic test image. This image contains the sum of a checkerboard pattern and a sinusoidal pattern of slightly higher spatial frequency. The checkerboard is intended to represent two tissue classes, while the spatial sinusoid is meant to represent an intensity inhomogeneity.

The initial segmentation appears on the right in Figure 1. This result is equivalent to that which would be obtained from a conventional two-class gaussian classifier operating on the synthetic image. The sinusoidal ‘inhomogeneity’ has clearly disturbed the classification.

Figure 2 shows the final segmentation and bias field that result from running the iteration to convergence. The method has succeeded in correcting and classifying the data.

This example would be difficult to correct using homomorphic filtering approaches to intensity correction, since the signal and contaminant are not well separated spectrally. Homomorphic filtering is discussed in more detail in Section 5.

3.1.2 Coronal Brain Slices

Slice Example Figure 3 shows the input image, a slice from a coronal 3DFT gradient-echo T1-weighted acquisition. The brain tissue ROI was generated manually. Figure 4 shows the initial white matter probabilities and segmentation. These results are equivalent to that which would be obtained using a conventional two-class gaussian classifier. Figure 5 shows the final white matter probabilities and segmentation resulting from adaptive segmentation. Figure 6 shows the final bias field estimate. The largest value of the input data was 85, while the difference between the largest and smallest values of the bias correction was about 10.

Note the significant improvement in the right temporal area. In the initial segmentation the white matter is completely absent in the binarization.

3D Example The method was used to segment a complete coronal data set consisting of 124 slices that are similar to the one described above.

In Figure 7 the exterior gray matter surface of the brain is shown for reference. This surface lies just inside the brain ROI, which was generated semi-automatically as in [11].

Figure 8 shows the white matter surface, as determined by adaptive segmentation while Figure 9 shows the result obtained without intensity correction, which is equivalent to that of conventional intensity-based segmentation. Note the generally ragged appearance and the absence of the temporal white matter structures.

The 3D renderings were generated using the dividing cubes algorithm [29].

3.1.3 Sagittal Slice obtained with Surface Coil

This section shows results obtained by using the method on a sagittal surface coil brain image. Surface coil images are frequently used in functional and interventional MRI because of their high signal-to-noise ratio in the vicinity of the coil, however, this type of data has severe intensity inhomogeneities. The five-inch receive-only surface coil was positioned at the back of the head. Figure 10 shows the intensity image in the upper position, after having been windowed for viewing the occipital area. Note that “optimal viewing” of the image in the occipital region prevents the visualization of the rest of the image. The lower position of Figure 10 shows the gray matter probabilities resulting from starting the algorithm on the “M” step and running for one cycle. This result is equivalent to that which might be obtained using linear methods of intensity correction, see Section 5 for additional discussion. A brain ROI was generated manually.

Figure 11 shows the final gray matter probability in the upper position and the final bias field estimate in the lower image. Figure 12 shows the corrected intensity image. Here the gain field estimate has been applied as a correction in the ROI. Note the dramatic improvement in “viewability” – the entire brain area is now visible, although (inevitably) the noise level is higher in the frontal brain tissue that is farthest from the surface coil. Also note that despite the serious gradient in the data the gray matter / white matter contrast is consistent in the entire corrected image.

3.2 Automated Segmentation of Double-Echo Spin-Echo MRI Data

The results shown in this section were obtained using the non-parametric extended method described in Sections 2.5 and 2.6.2.

3.2.1 Double-Echo Axial Example

This section demonstrates results for one slice of a double-echo axial acquisition of a normal volunteer.

Figure 13 shows one slice of registered proton-density and T2-weighted images. The corresponding initial and final segmentations are shown in Figure 14 in the upper and lower positions, respectively. The tissues are encoded from black to white as follows: background, subcutaneous fat, CSF, gray matter, white matter. The initial segmentation is substantially erroneous because of static gain discrepancies between the tissue intensity models and the data, in addition to spatial inhomogeneities. This result is equivalent to that which would be obtained with conventional non-parametric segmentation [23]. The

final segmentation shows that the method has been able to adapt to the intensities present in the data. We have found that the method can reliably segment such MRI data across patients and equipment upgrades without any adjustment or intervention.

Figures 15 and 16 show the final weights for selected tissue classes. As pointed out in Section 2.2, these weights are a good indicator of tissue class. The final segmentation was obtained by choosing the tissue class with the largest weight at each voxel.

3.2.2 Multiple Sclerosis Data

This section describes results recently obtained for segmenting MR images from a large, longitudinal study of several dozen patients with multiple sclerosis (MS) [30].

Figures 17 and 18 show a sequence of registered proton-density and T2-weighted images for a single multiple-sclerosis patient with multiple white matter lesions. These images represent the same section from 20 scans over time after they were spatially registered using the method described in [31, 32].

The same tissue class conditional intensity models were used to segment all sections. The results without intensity correction are shown in Figure 19. Tissues are encoded from black to white as follows: background, subcutaneous fat, gray matter, CSF, lesions, white matter. These results are equivalent to those which would be obtained using conventional non-parametric intensity-based segmentation (which would more typically be used with per-scan manual training). These results show many gross misclassifications and demonstrate that conventional intensity-based segmentation is unfeasible in this application, at least without per-scan training. Even with per-scan training, significant asymmetries will remain in the results due to the spatial intensity inhomogeneities present in the data. Results using adaptive segmentation are shown in Figure 20 using the same tissue encoding. Good stability and symmetry of the cortical gray matter structures are apparent. Similar results have been obtained in processing 23 complete scans for each of 47 patients participating in the study mentioned above, without the need for retraining or manually-generating regions-of-interest. This has facilitated monitoring the evolution of specific white matter lesions over time. Thus, fully automatic segmentation of clinical MRI data has been demonstrated in more than 1000 complete scans, without the need for per-patient or per-scan training or adjustments. The exams occurred over a 2.5 year period that included a major MR equipment upgrade.

4 Comparison to Manual and Supervised Segmentation

This section describes a comparison of adaptive segmentation to manual and supervised segmentation methods in segmenting white matter and gray matter. The single-channel

implementation that is described in Sections 2.4 and 2.6.1 was used. In the first test, adaptive segmentation was compared to manual segmentations (outlining of structures performed by experienced raters). In the second test, adaptive segmentation was compared to supervised multivariate classification. The images, manual segmentations, and supervised segmentations are described in [23].

Adaptive segmentation was applied to a single slice of an axial proton-density spin-echo image, using a brain-tissue ROI. The ROI was obtained by selecting those pixels that were labeled as brain tissue by four of the five raters in the manual segmentations. The amount of difference between segmentations was calculated as the percentage of pixels in the ROI having different labels.

4.1 Comparison to Manual Segmentation

Table 1 shows the results of comparing the method to segmentations performed manually by experienced raters. The percentage of difference within the brain ROI is shown for comparisons within a group consisting of the manual segmentations and the segmentation resulting from Adaptive Segmentation. The percentage of difference between two segmentations was calculated by dividing the number of differently labeled pixels within the ROI by the total number of pixels within the ROI. The lower part of the table shows the average of the percentages of difference from the other segmentations. The adaptive segmentation is consistent with the manual segmentations in the sense that it does not have the largest average difference.

4.2 Comparison to Supervised Classification

Table 2 shows the results of comparing the method to segmentations performed by the same expert raters using a supervised segmentation method described in [23]. In this test, percentages of difference within the ROI are displayed for comparisons of the supervised segmentations and the adaptive segmentations with the manual segmentations described above. The average percentage of difference (calculated as above) from the manual segmentations is also shown. The adaptive segmentation is seen to have less average difference from the manual segmentations than the supervised segmentations, so in this test, its performance is better.

5 Discussion

The algorithm that has been described has two components, estimation of tissue class probability, and gain field estimation. Our contribution has been to combine them in an

	Rater A	Rater B	Rater C	Rater D	Rater E	Adaptive
Rater A	0.0	13.97	20.64	15.82	12.72	21.33
Rater B	13.97	0.0	22.16	15.99	15.11	20.67
Rater C	20.64	22.16	0.0	23.25	20.14	19.45
Rater D	15.82	15.99	23.25	0.0	15.30	23.02
Rater E	12.72	15.11	20.14	15.30	0.0	20.71
Adaptive	21.33	20.67	19.45	23.02	20.71	0.0
Average	16.90	17.58	21.13	18.58	16.80	21.04

Table 1: Percentage Differences among Manual and Adaptive Segmentations: Adaptive Segmentation is Consistent with Manual Segmentations

Manual Segmentation by	Supervised Segmentation by					Adaptive
	Rater A	Rater B	Rater C	Rater D	Rater E	
Rater A	25.22	22.52	23.04	22.51	22.29	21.33
Rater B	23.86	21.43	21.45	21.32	20.92	20.67
Rater C	19.55	21.19	18.21	21.08	18.13	19.45
Rater D	27.45	25.68	25.78	25.47	25.08	23.02
Rater E	24.61	23.15	22.75	22.87	22.11	20.71
Average	24.15	22.79	22.25	22.65	21.71	21.04

Table 2: Percentages of Difference from Manual Segmentations of Supervised and Adaptive Segmentations: Adaptive Segmentation shows better Agreement with Manual Segmentation than Supervised Segmentation

iterative scheme that yields a powerful new method for estimating both tissue class and gain field.

The use of multi-channel statistical intensity classifiers was pioneered by Vannier et al.[8]. The classification component of adaptive segmentation is similar to the method described by Gerig et al. and Cline et al. [10, 11]. They used Maximum-Likelihood classification of voxels using normal models with two-channel MR intensity signals and a semi-automatic way of isolating the brain using connectivity. The classification component of the non-parametric extended method is equivalent to that described [23].

The bias field estimation component of adaptive segmentation method is somewhat similar to homomorphic filtering (HMF) approaches that have been reported. Lufkin et al. [12] and Axel et al. [13] describe approaches for controlling the dynamic range of surface-coil MR images. A low-pass-filtered version of the image is taken as an estimate of the gain field, and used to correct the image. Lim and Pfferbaum [14] use a similar approach to filtering that handles the boundary in a novel way, and apply intensity-based segmentation to the result.

When started on the “M Step”, and run for one cycle, adaptive segmentation is equivalent to HMF followed by conventional intensity-based segmentation. We have discovered, however, that more than one iteration are frequently needed to converge to good results – indicating that adaptive segmentation is more powerful than HMF followed by intensity-based segmentation. The essential difference is that adaptive segmentation utilizes evolving knowledge of the tissue type to make increasingly accurate estimates of the gain field.

Dawant, Zijdenbos and Margolin describe methods for correcting intensities for tissue classification [15]. In one variant, an operator selected points of a tissue class are used to regress an intensity correction. In the other method, a preliminary segmentation is used in determining an intensity correction, which is then used for improved segmentation. This strategy is somewhat analogous to starting adaptive segmentation on the “E step” and running it for one and a half cycles. As in the previous case, our results demonstrate improvement with additional iterations.

Aylward and Coggins describe a two-stage approach that first uses a band-pass intensity corrector. Remaining inhomogeneities are handled by using supervised training to obtain spatially-varying statistics for classifying the corrected MR data [17].

Several authors have reported methods based on the use of phantoms for intensity calibration [13, 16]. This approach has the drawback that the geometric relationship of the coils and the image data is not typically available with the image data (especially with surface coils). Fiducial markers were used to address this problem in [16]. In addition, the calibration approach can become complicated because the response of tissue to varying amounts of RF excitation is significantly non-linear (see [33, Equations 1-3 and 1-16]). In addition, phantom calibration cannot account for possible gain inhomogeneities induced

by the interaction of anatomy and the RF coils.

The present work has focused on the correction of intensity inhomogeneities in MR. The correction of *magnetic field* inhomogeneities of MR images has received considerable attention. Such inhomogeneities can cause significant geometrical distortions. An effective in-vivo correction approach is described in [34].

6 Conclusions

We have demonstrated a new fully-automatic method, called adaptive segmentation, for segmenting and intensity-correcting MR images.

Adaptive segmentation increases the robustness and level of automation available for the segmentation of MR images into tissue classes by correcting intra- and inter-scan intensity inhomogeneities. Via improved segmentation, the approach leads to improved automatic 3D reconstruction of anatomical structures, for visualization, surgical planning, disease research, drug therapy evaluation, anatomical reference and other purposes.

Adaptive segmentation also facilitates the post-processing of medical MR images for improved appearance by correcting intensity inhomogeneities present in the image. This is especially useful for images derived from surface coils, where the large intensity variations make it difficult to accommodate the image data on films for viewing.

7 Acknowledgments

We thank Maureen Ainsle, Mark Anderson, Ihan Chou, Gil Ettinger, Langham Gleason, Charles Guttmann, Steve Hushek, Hiroto Hokama, Tina Kapur, Sanjeev Kulkarni, Robert McCARley, Martha Shenton, Simon Warfield and Cynthia Wible for contributions to this paper.

References

- [1] M. Shenton, R. Kikinis, F. Jolesz, et al. Abnormalities of the Left Temporal Lobe and Thought Disorder in Schizophrenia. *N. Engl. J. Med.*, (327):604–612, 1992.
- [2] K. Höhne et al. A framework for the Generation of 3D Anatomical Atlases. In *SPIE Vol. 1808, Visualization in Biomedical Computing 1992*, 1992.
- [3] R. Kikinis, F.A. Jolesz, W.E. Lorensen, H.E. Cline, P.E Stieg, and P. McL. Black. 3d Reconstruction of Skull Base Tumors from MRI Data for Neurosurgical Planning. In *Proceedings of the Society of Magnetic Resonance in Medicine Conference*, 1991.

- [4] R. Kikinis, D. Altobelli, W. Lorensen, W. Wells, and G. Ettinger. Pre- and intra-operative tumor localization using 3d renderings of mri's. In *Abstracts of the 12th Annual Scientific Meeting of the Society of Magnetic Resonance in Medicine*, 1993.
- [5] D. Levin, X. Hu, K. Tan, et al. The Brain: Integrated Three-Dimensional Display of MR and PET Images. *Radiology*, (172):783 – 789, 1989.
- [6] J. Belliveau, D. Kennedy, R. McKinstry, et al. Functional Mapping of the Human Visual Cortex by Magnetic Resonance Imaging. *Science*, 254:716–719, November 1991.
- [7] J. Bezdek, L. Hall, and L. Clarke. Review of MR Image Segmentation Techniques using Pattern Recognition. *Medical Physics*, 20(4):1033 – 1048, 1993.
- [8] M. Vannier, R. Butterfield, D. Jordan, W. Murphy, et al. Multi-Spectral Analysis of Magnetic Resonance Images. *Radiology*, (154):221 – 224, 1985.
- [9] M. Kohn, N. Tanna, G. Herman, et al. Analysis of Brain and Cerebrospinal Fluid Volumes with MR Imaging. *Radiology*, (178):115 – 122, 1991.
- [10] G. Gerig, W. Kuoni, R. Kikinis, and O. Kübler. Medical Imaging and Computer Vision: an Integrated Approach for Diagnosis and Planning. In *Proc. 11'th DAGM Symposium*, pages 425–443. Springer, 1989.
- [11] H.E. Cline, W.E. Lorensen, R. Kikinis, and F. Jolesz. Three-Dimensional Segmentation of MR Images of the Head Using Probability and Connectivity. *JCAT*, 14(6):1037–1045, 1990.
- [12] R.B. Lufkin, T. Sharpless, B. Flannigan, and W. Hanafee. Dynamic-Range Compression in Surface-Coil MRI. *AJR*, 147(379):379–382, 1986.
- [13] L. Axel, J. Costantini, and J. Listerud. Intensity Correction in Surface-Coil MR Imaging. *AJR*, 148(4):418–420, 1987.
- [14] K.O. Lim and A. Pfferbaum. Segmentation of MR Brain Images into Cerebrospinal Fluid Spaces, White and Gray Matter. *JCAT*, 13(4):588–593, 1989.
- [15] B. Dawant, A. Zijdenbos, and R. Margolin. Correction of Intensity Variations in MR Images for Computer-Aided Tissue Classification. *IEEE Trans. Med. Imaging*, 12(4):770 – 781, 1993.
- [16] J. Gohagan, E. Spitznagel, W. Murphy, M. Vannier, et al. Multispectral Analysis of MR Images of the Breast. *Radiology*, (163):703 – 707, 1987.

- [17] S. Aylward and J. Coggins. Spatially Invariant Classification of Tissues in MR Images. In *Proceedings of the Third Conference on Visualization in Biomedical Computing*. SPIE, 1994.
- [18] M. Kamber, D. Collins, R. Shinghal, G. Francis, and A. Evans. Model-Based 3D Segmentation of Multiple Sclerosis Lesions in Dual-Echo MRI Data. In *SPIE Vol. 1808, Visualization in Biomedical Computing 1992*, 1992.
- [19] A.P. Dempster, N.M. Laird, and D.B. Rubin. Maximum Likelihood from Incomplete Data via the EM Algorithm. *J. Roy. Statist. Soc.*, 39:1 – 38, 1977.
- [20] J.S. Lim. *Two-Dimensional Signal and Image Processing*. Prentice Hall, 1990.
- [21] B.R. Frieden. *Probability, Statistical Optics, and Data Testing*. Springer-Verlag, 1983.
- [22] W. Wells, R. Kikinis, W. Grimson, and F. Jolesz. Statistical Intensity Correction and Segmentation of Magnetic Resonance Image Data. In *Proceedings of the Third Conference on Visualization in Biomedical Computing*. SPIE, 1994.
- [23] R. Kikinis, M. Shenton, F.A. Jolesz, G. Gerig, J. Martin, M. Anderson, D. Metcalf, C. Guttmann, R.W. McCarley, W. Lorensen, and H. Cline. Quantitative Analysis of Brain and Cerebrospinal Fluid Spaces with MR Imaging. *JMRI*, 2:619–629, 1992.
- [24] R.O. Duda and P.E. Hart. *Pattern Classification and Scene Analysis*. John Wiley and Sons, 1973.
- [25] W.M. Wells III. Efficient Synthesis of Gaussian Filters by Cascaded Uniform Filters. *IEEE Transactions PAMI*, PAMI-8(2):234 – 239, March 1986.
- [26] Sun Microsystems Inc., Mountain View, CA.
- [27] General Electric Medical Systems, Milwaukee, WI.
- [28] G. Gerig, O. Kübler, and F. Jolesz. Nonlinear Anisotropic Filtering of MRI data. *IEEE Trans. Med. Imaging*, (11):221–232, 1992.
- [29] H. Cline, W. Lorensen, S. Ludke, C. Crawford, and B. Teeter. Two Algorithms for the Three-Dimensional Reconstruction of Tomograms. *Med. Phys.*, (15):320 – 327, 1988.
- [30] Ron Kikinis et al. in preparation.

- [31] G. Ettinger, W. Grimson, T. Lozano-Pérez, W. Wells, S. White, and R. Kikinis. Automatic Registration for Multiple Sclerosis Change Detection. In *Proceedings of the IEEE Workshop on Biomedical Image Analysis*, Seattle, WA., 1994. IEEE.
- [32] W.E.L. Grimson, T. Lozano-Pérez, W. Wells, et al. An Automatic Registration Method for Frameless Stereotaxy, Image Guided Surgery, and Enhanced Reality Visualization. In *Proceedings of the Computer Society Conference on Computer Vision and Pattern Recognition*, Seattle, WA., June 1994. IEEE.
- [33] D. Stark and Jr. W. Bradley, editors. *Magnetic Resonance Imaging*. Mosby Year Book, 1992.
- [34] E. Schneider and G.H. Glover. Rapid In-Vivo Proton Shimming. *Magn. Resonance in Med.*, 18:335–347, 1991.

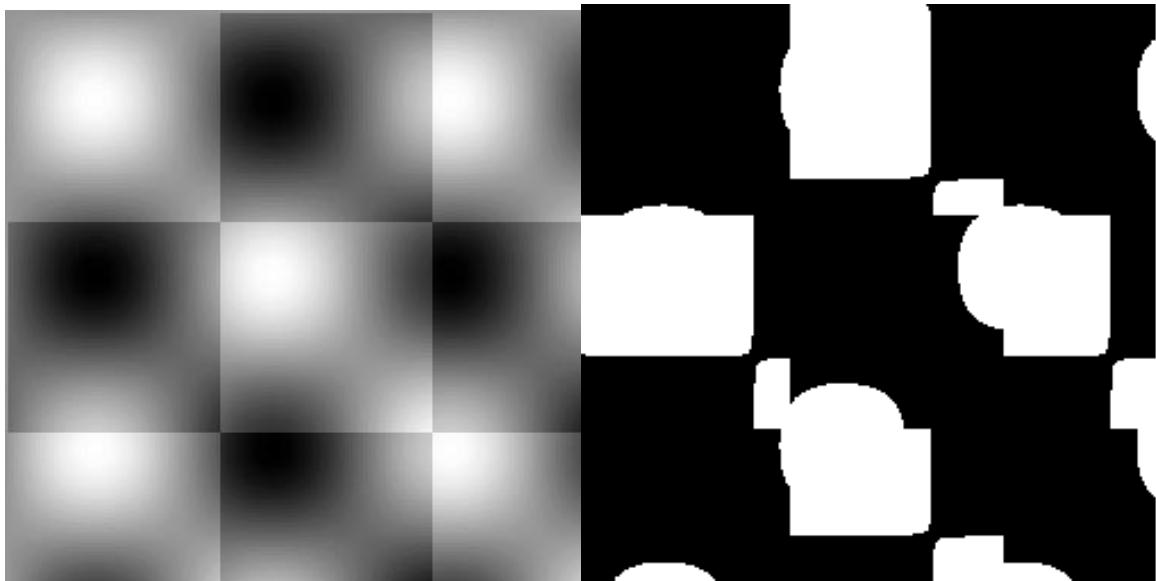


Figure 1: Synthetic image and results of conventional segmentation

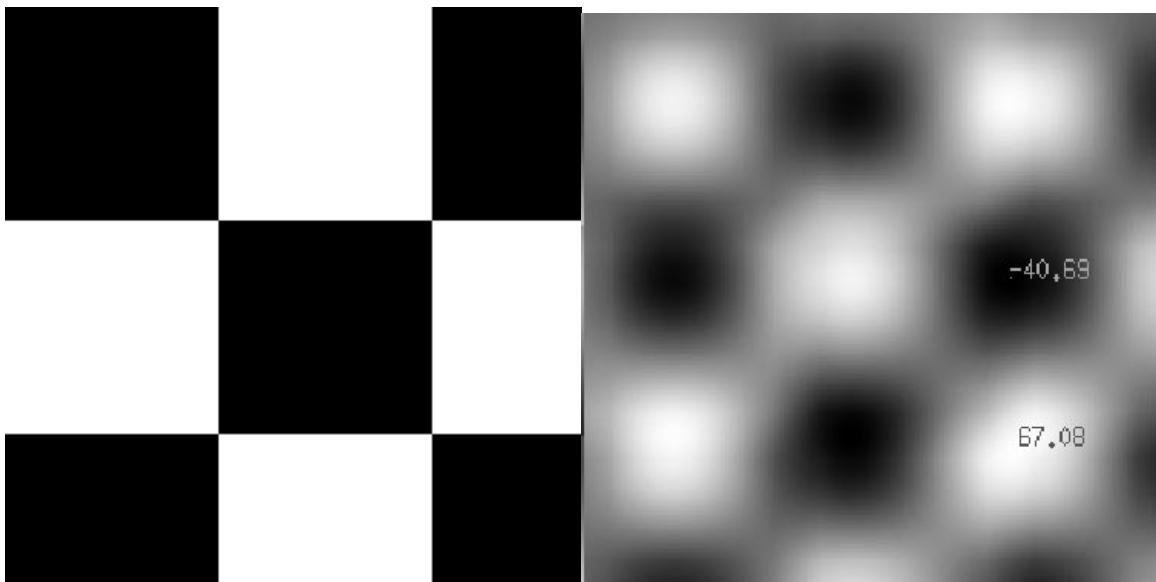


Figure 2: Results of adaptive segmentation and bias field

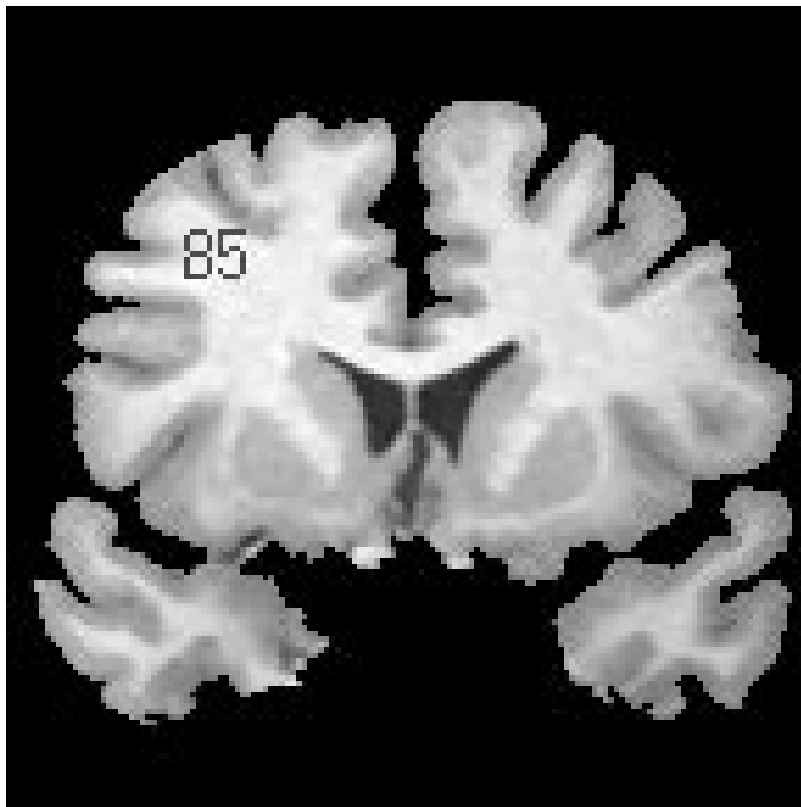


Figure 3: Original gradient-echo image.

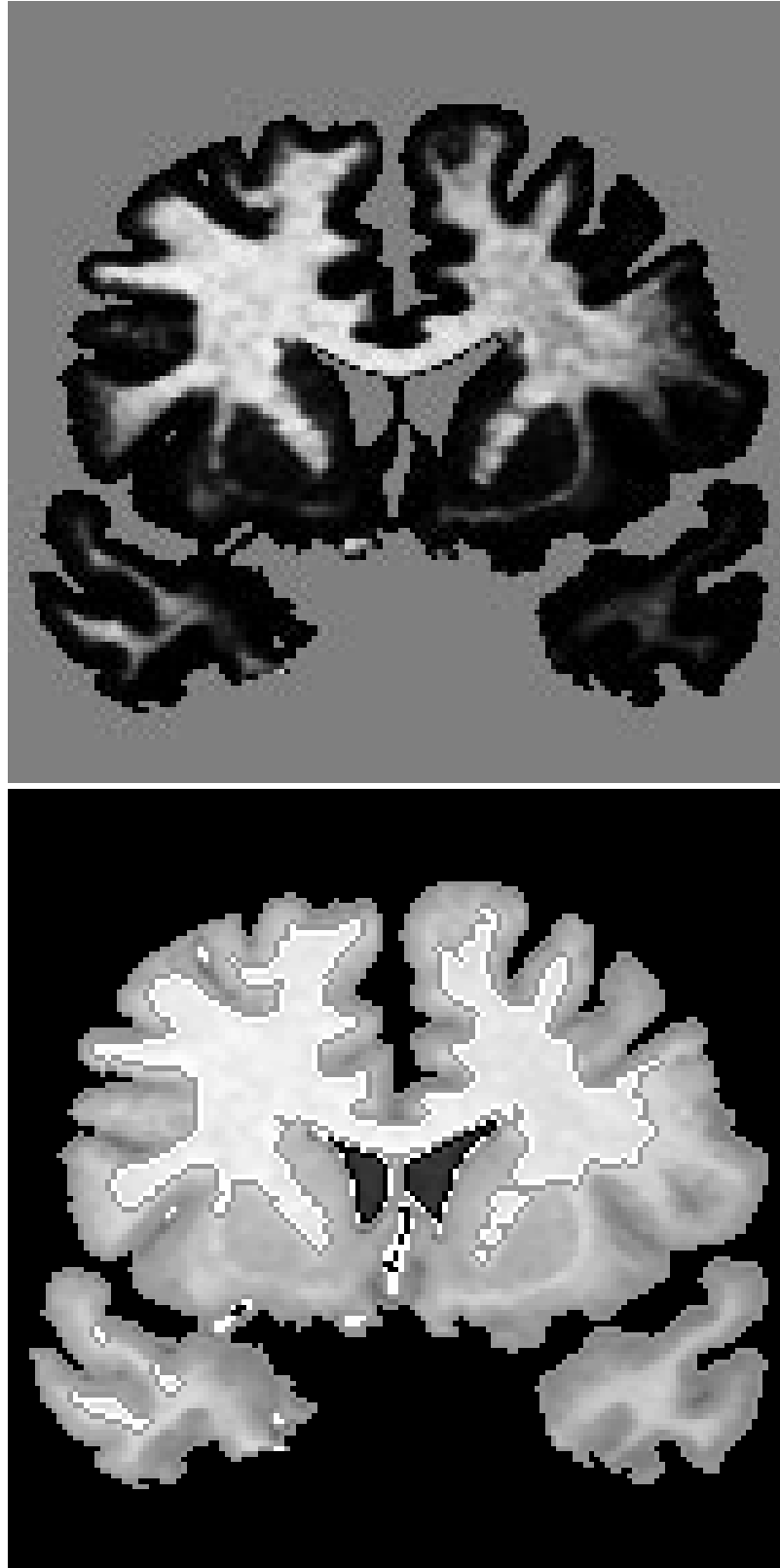


Figure 4: Results of conventional two-class Gaussian segmenter: white matter probability and segmentation

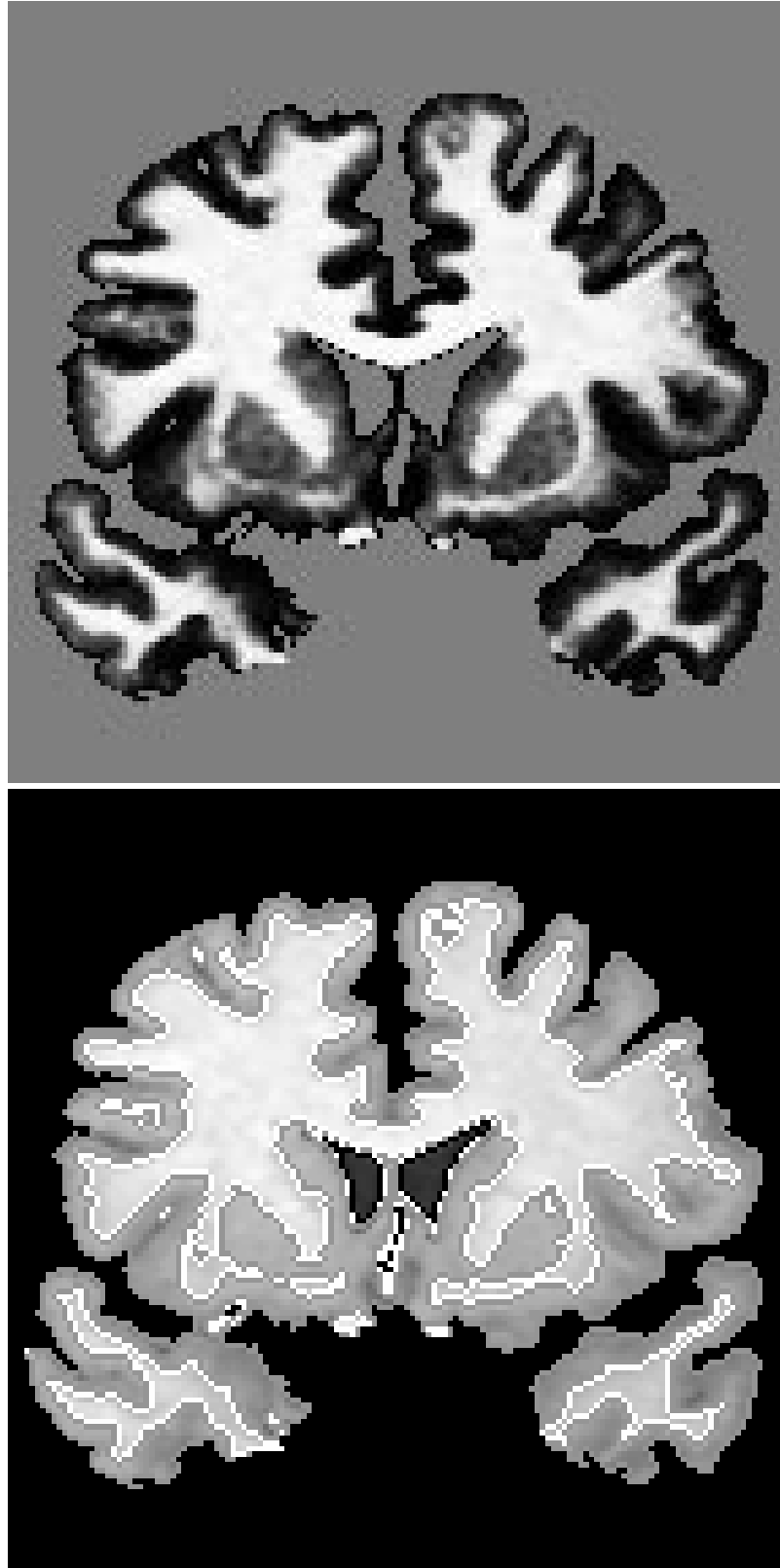


Figure 5: Results of adaptive segmentation: white matter probability and segmentation

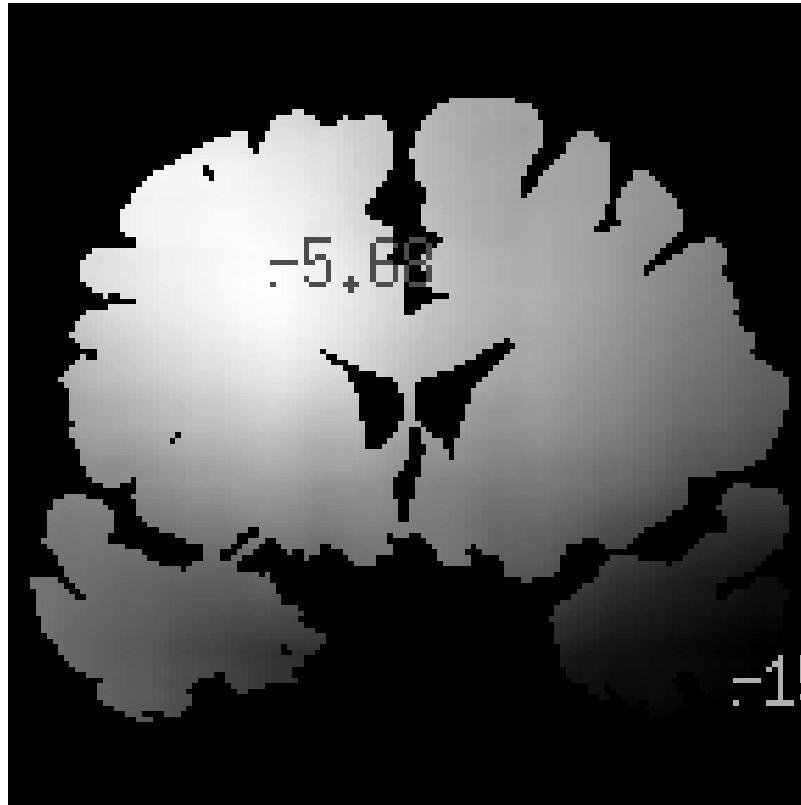


Figure 6: Estimated bias field

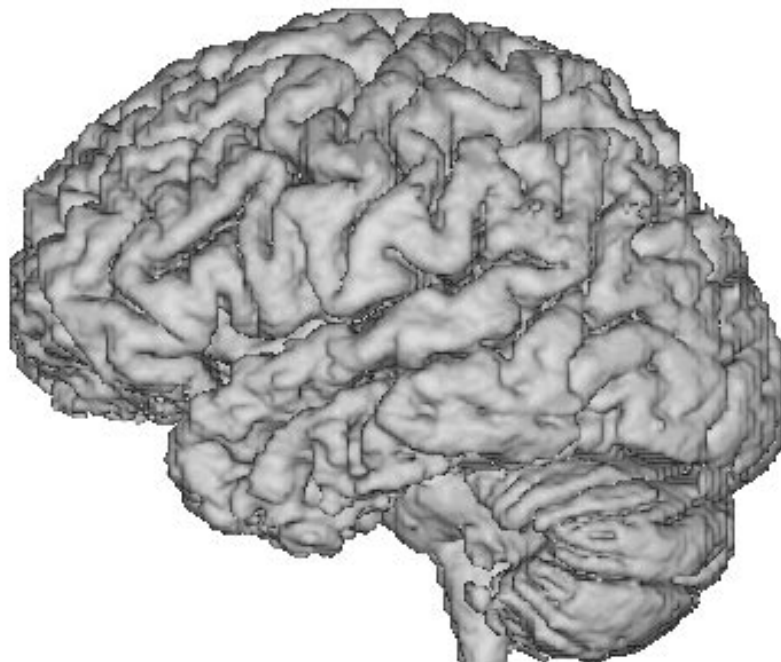


Figure 7: Gray matter surface

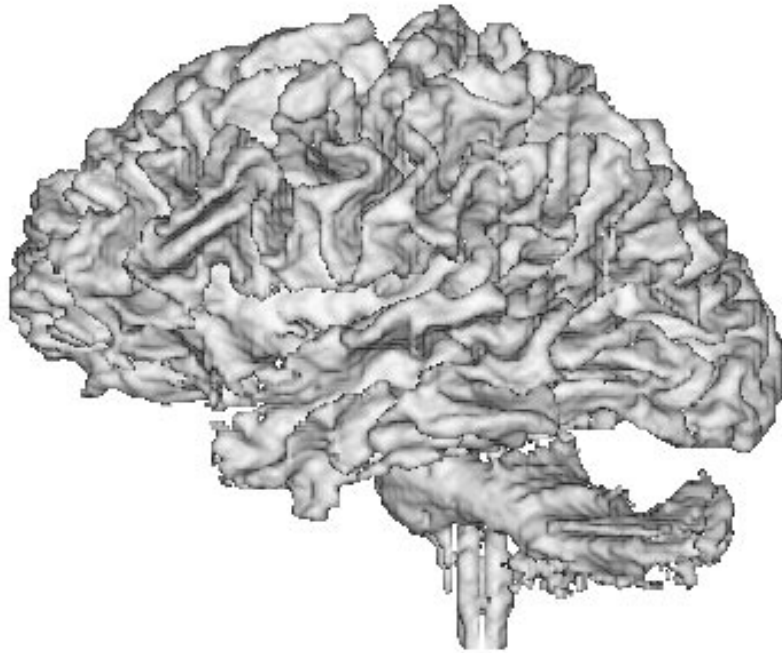


Figure 8: White matter surface determined by adaptive segmentation

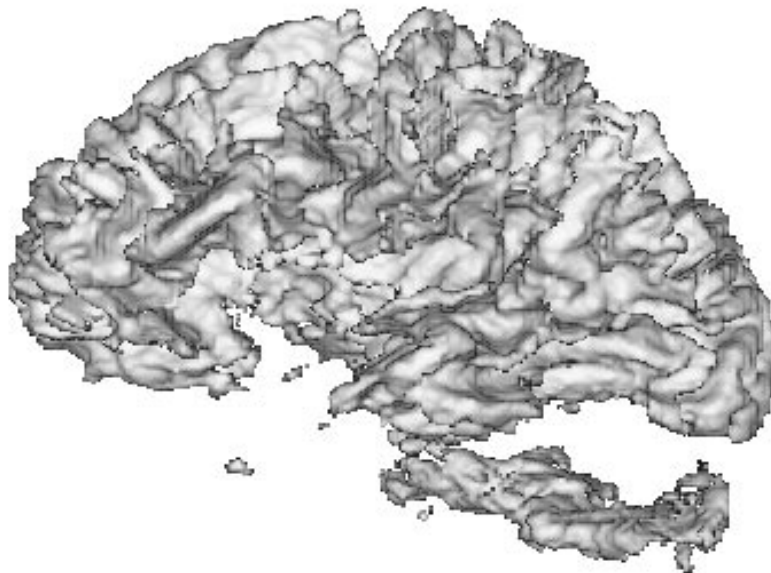


Figure 9: White matter surface determined by conventional intensity-based segmentation

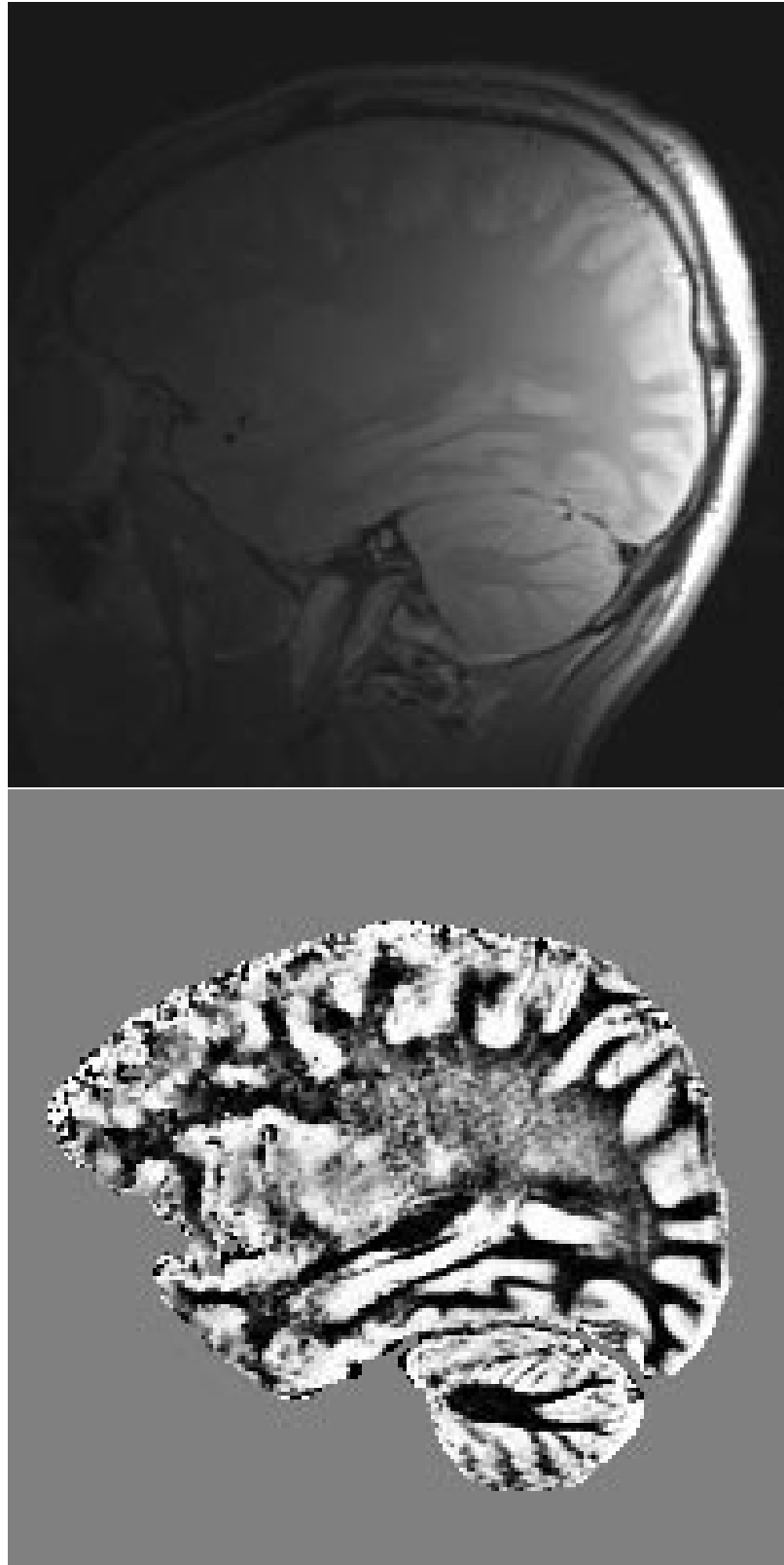


Figure 10: Surface-coil image and initial gray matter probability (equivalent to the use of a linear method of intensity correction)

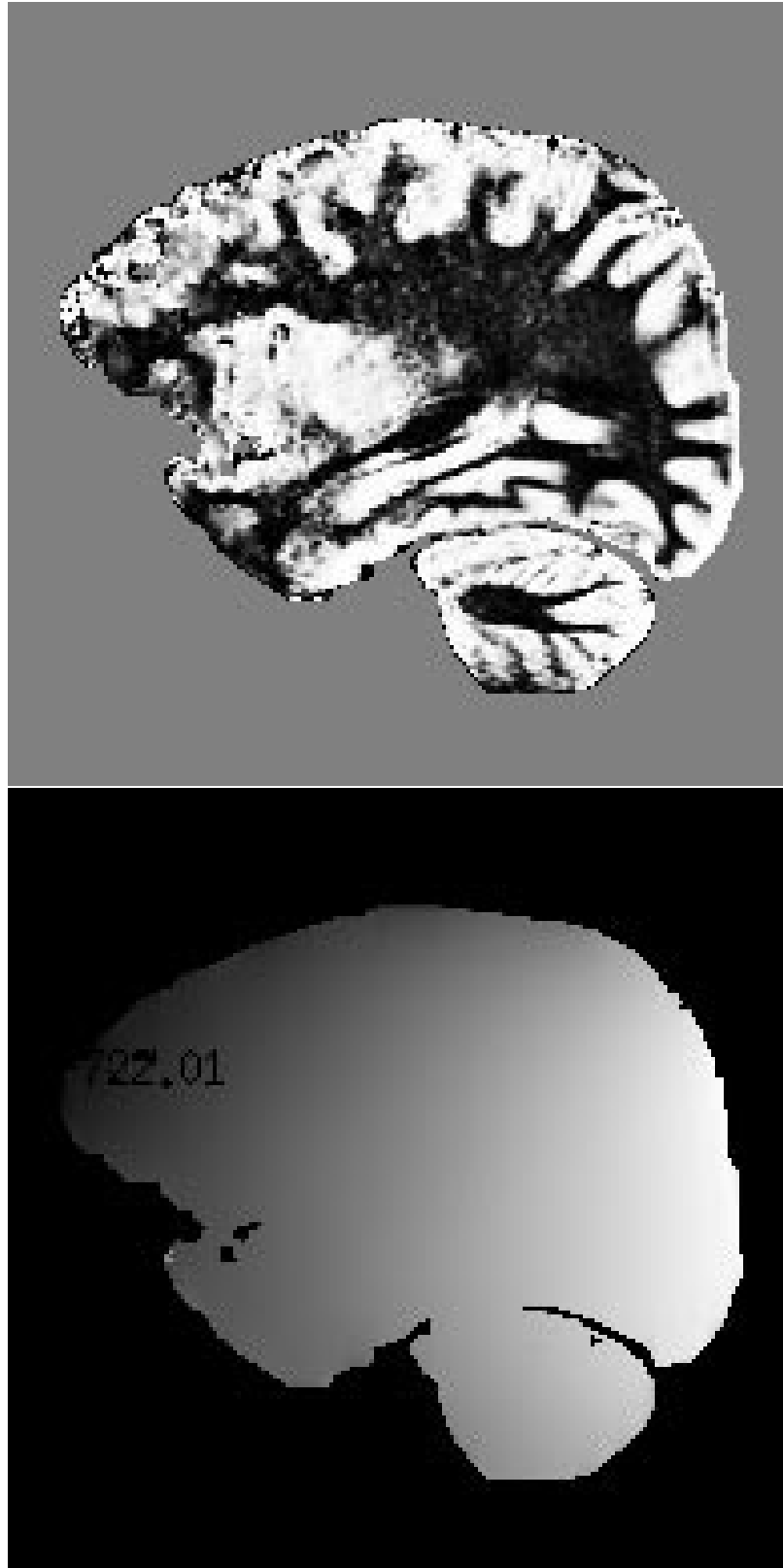


Figure 11: Results of adaptive segmentation: gray matter probability and bias estimate

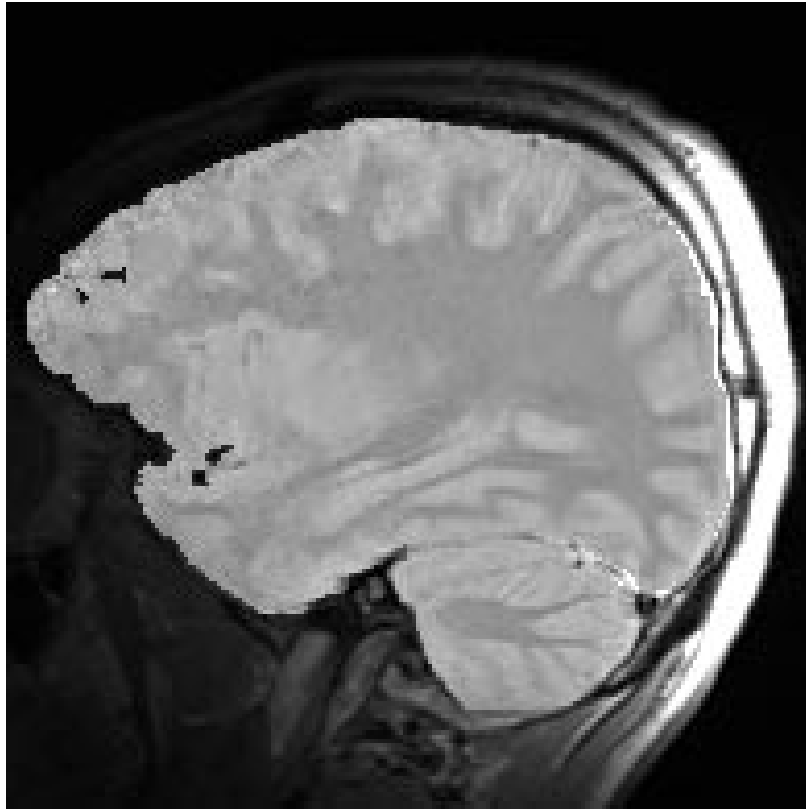


Figure 12: Results of adaptive segmentation: corrected image

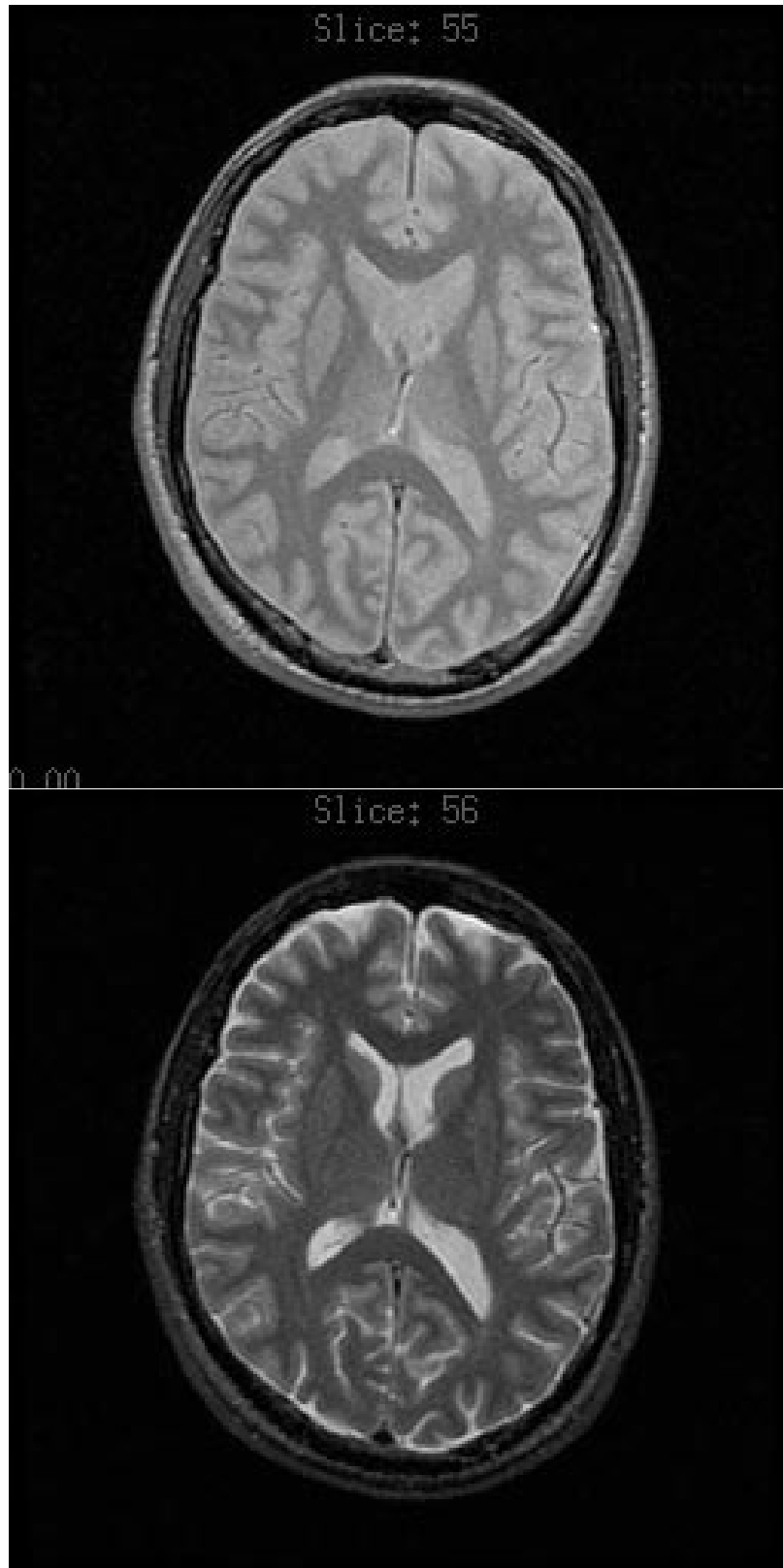


Figure 13: Proton-density and T2-weighted images

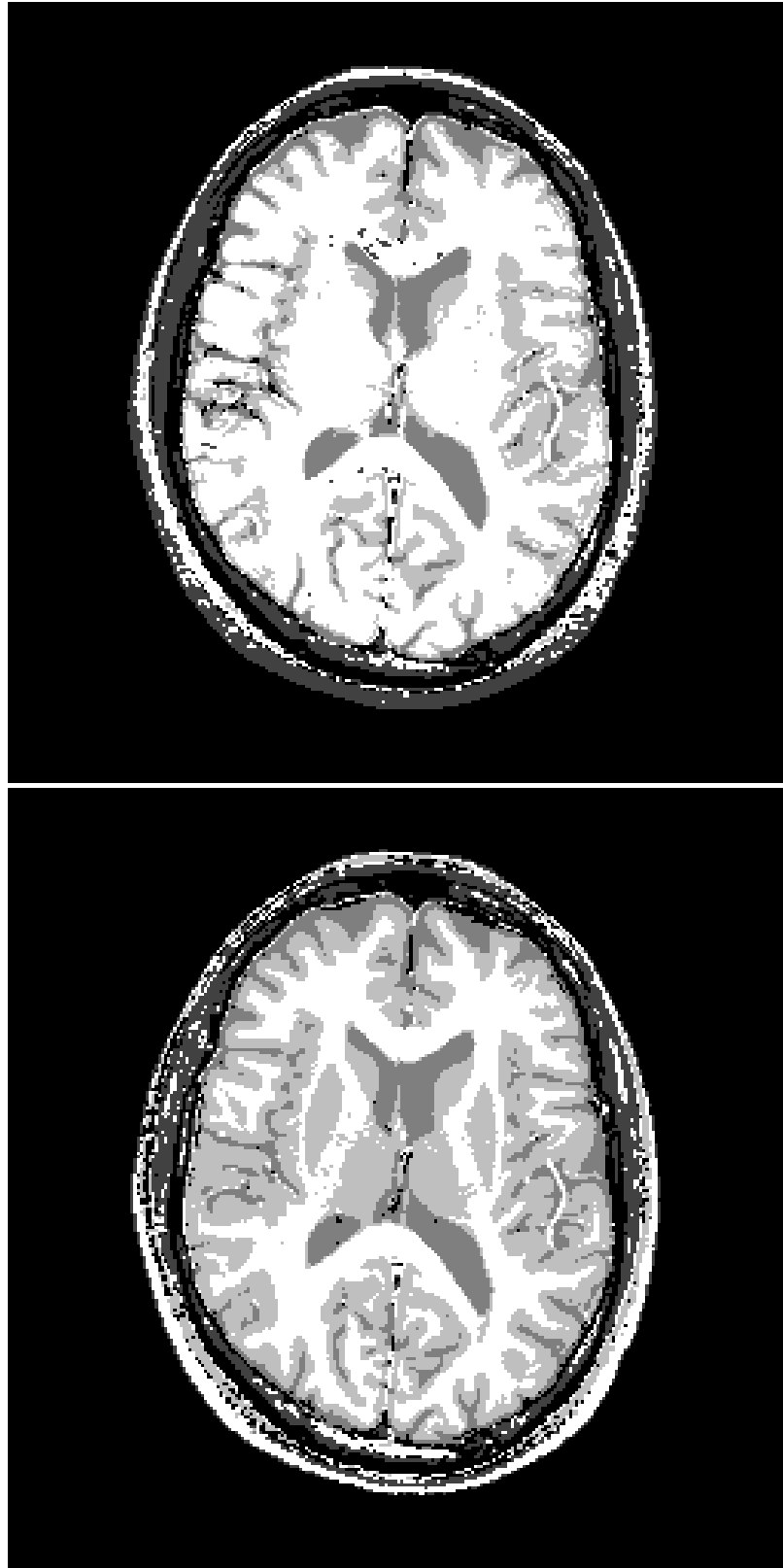


Figure 14: Results of conventional non-parametric segmentation and adaptive segmentation

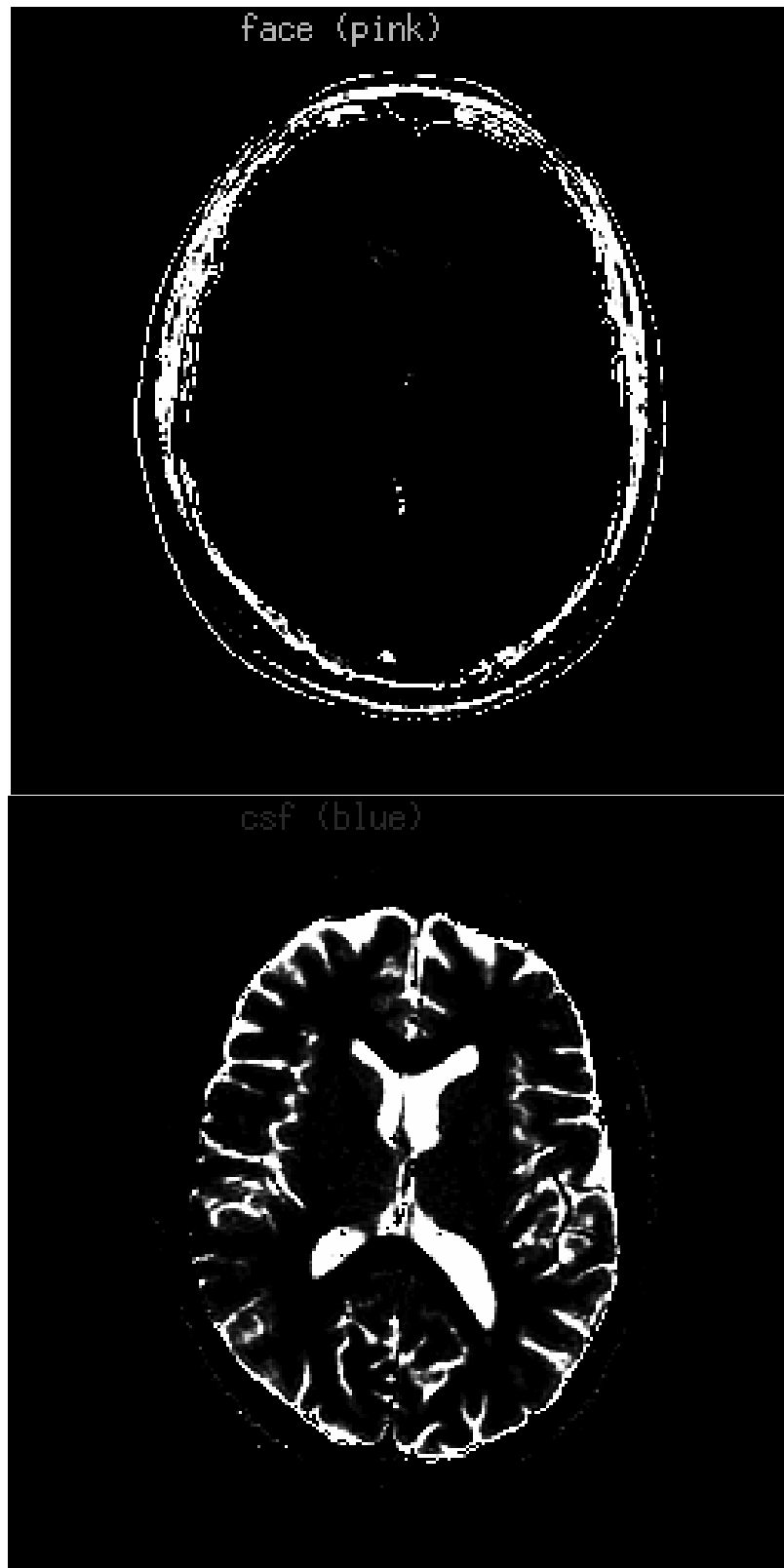


Figure 15: Weights for fat and CSF

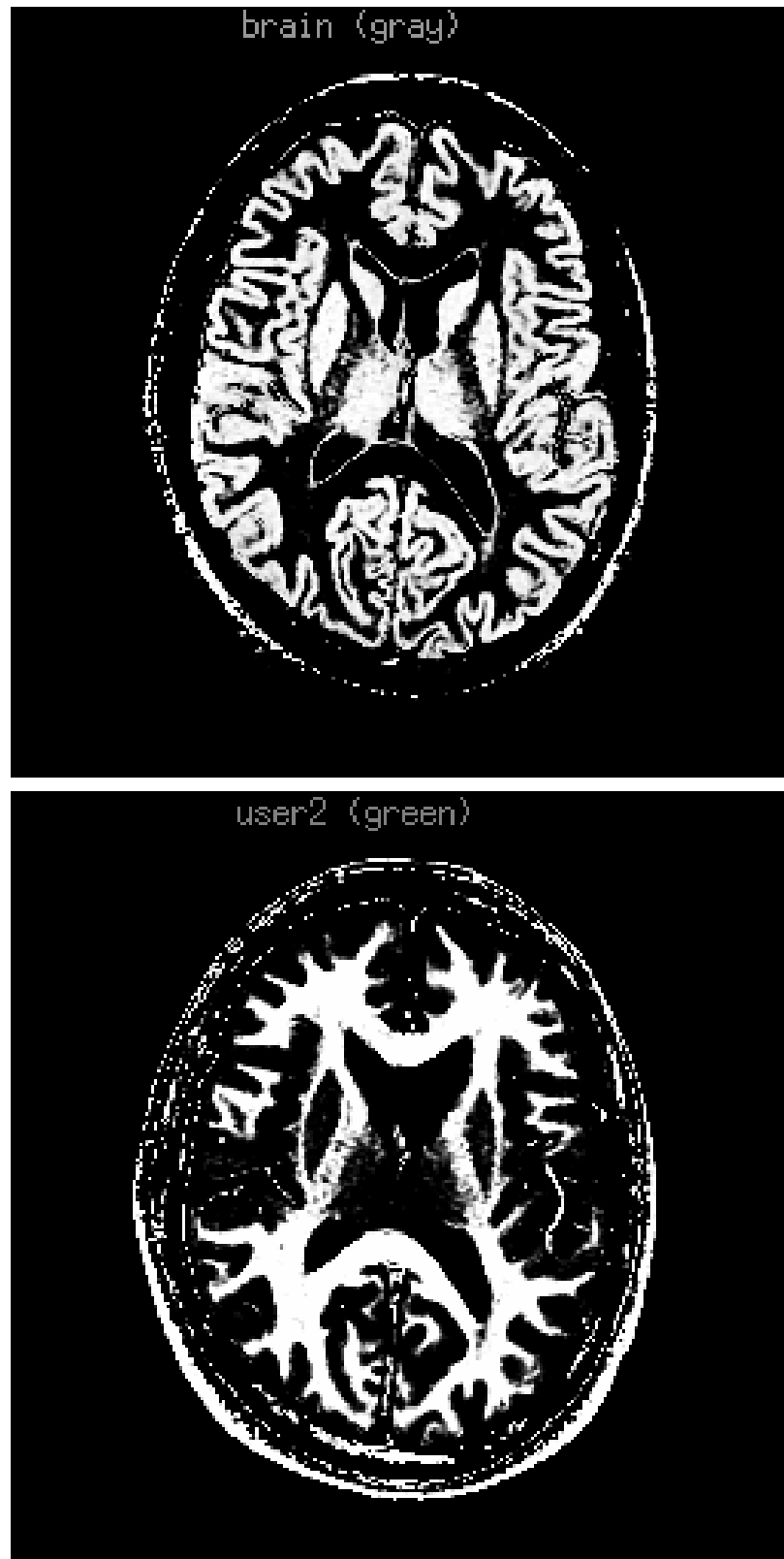


Figure 16: Weights for gray matter and white matter

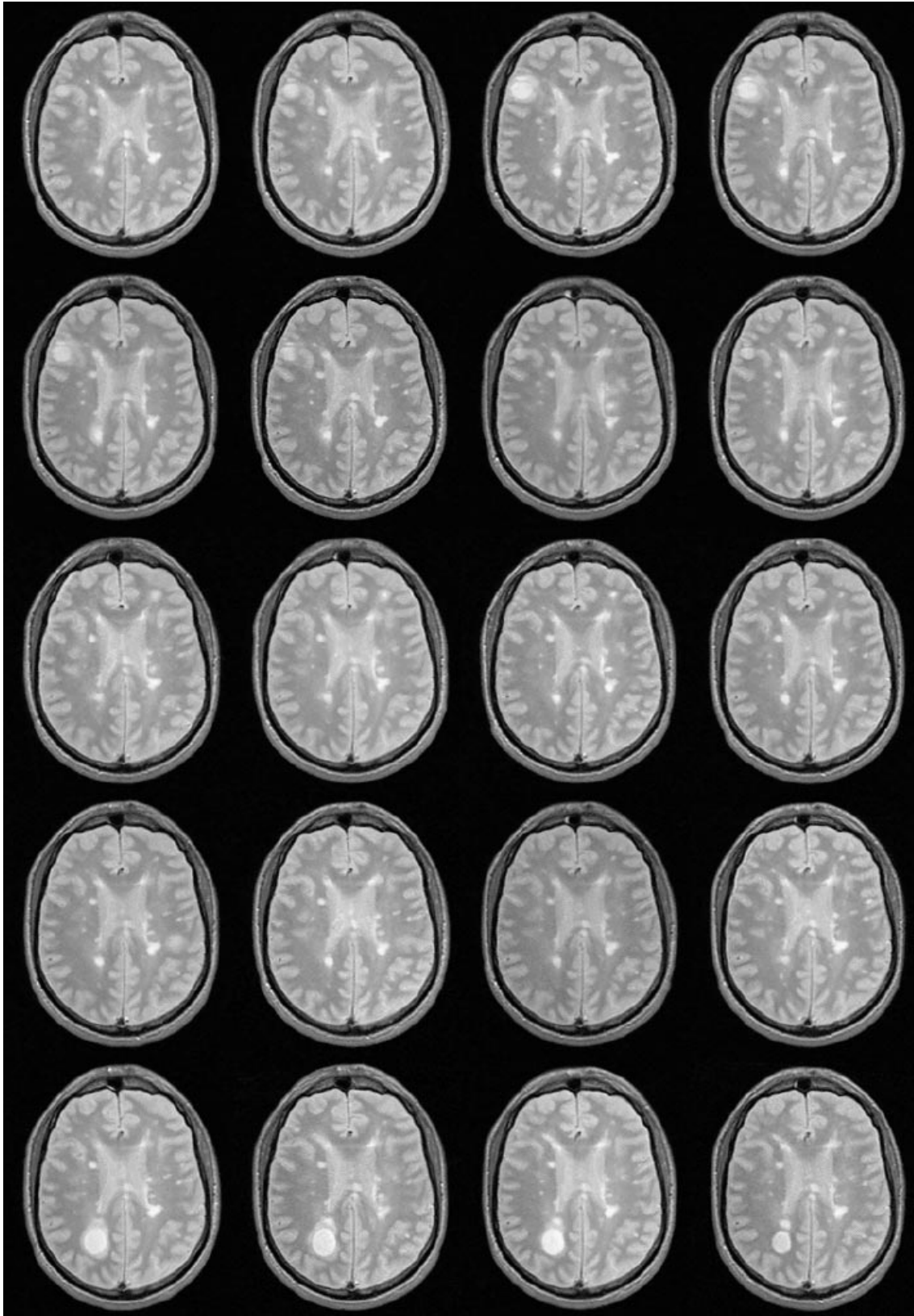


Figure 17: Multiple sclerosis data: registered proton-density images

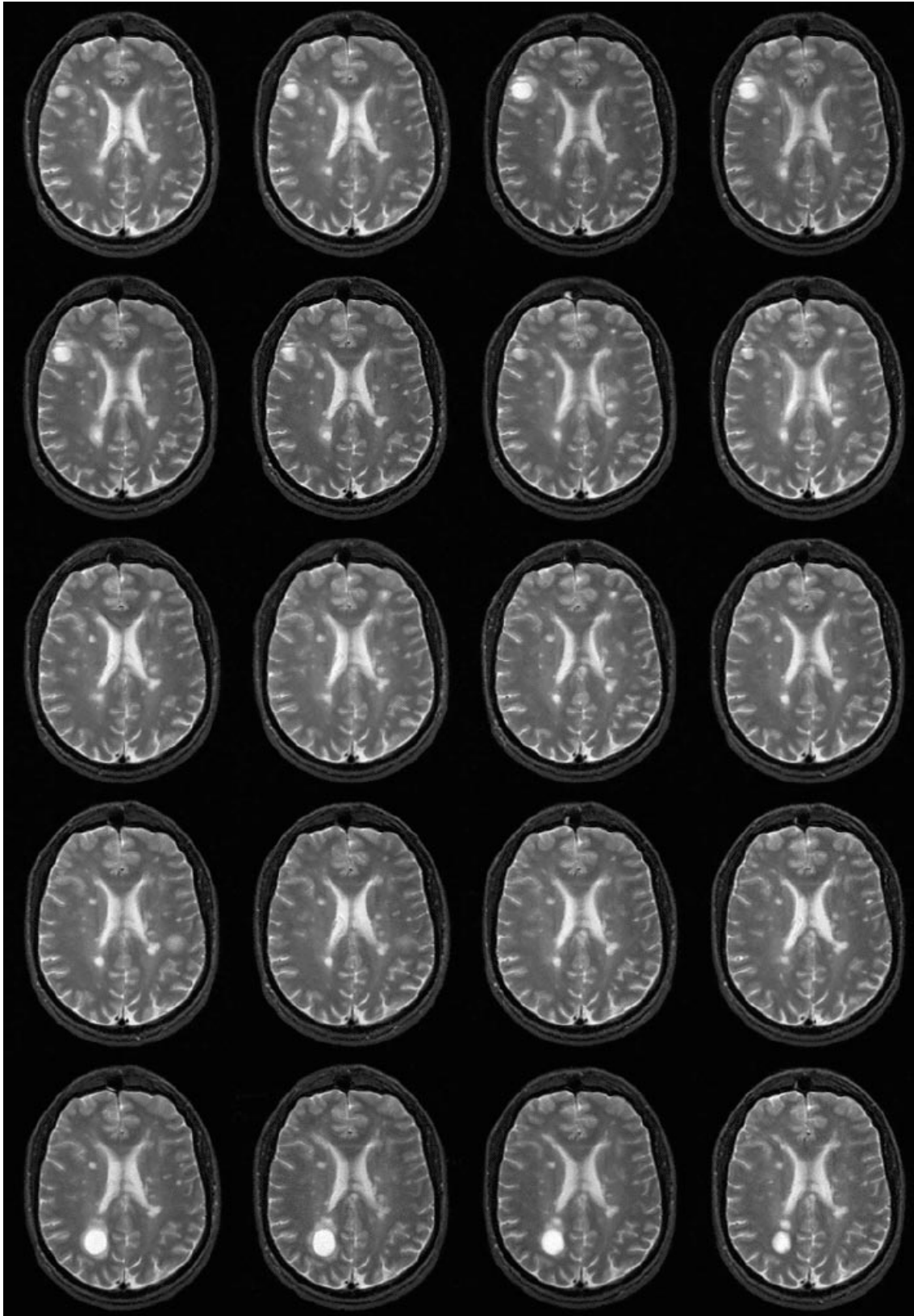


Figure 18: Multiple sclerosis data: registered T2-weighted images

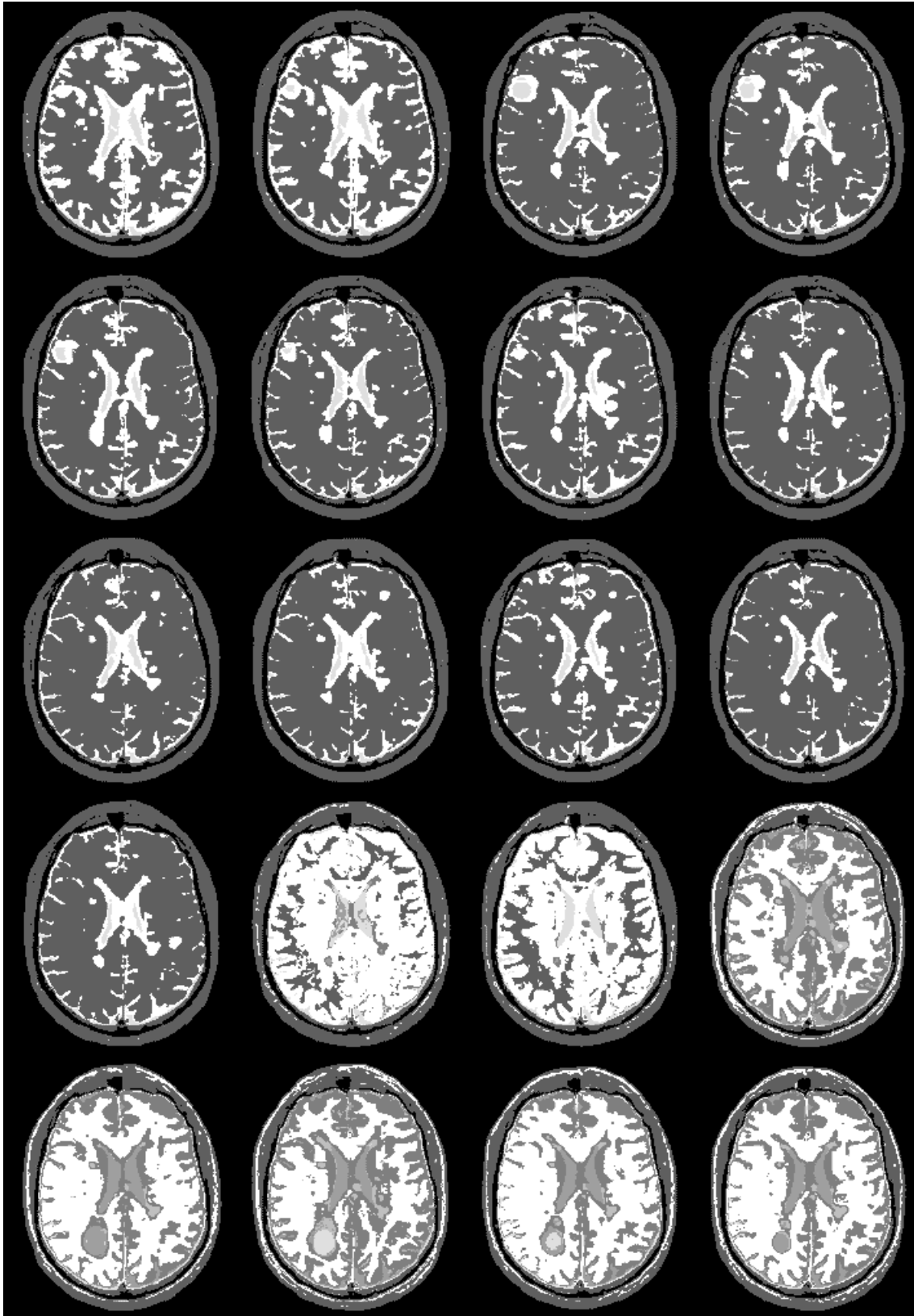


Figure 19: Conventional non-parametric intensity-based segmentation results (without per-scan training)

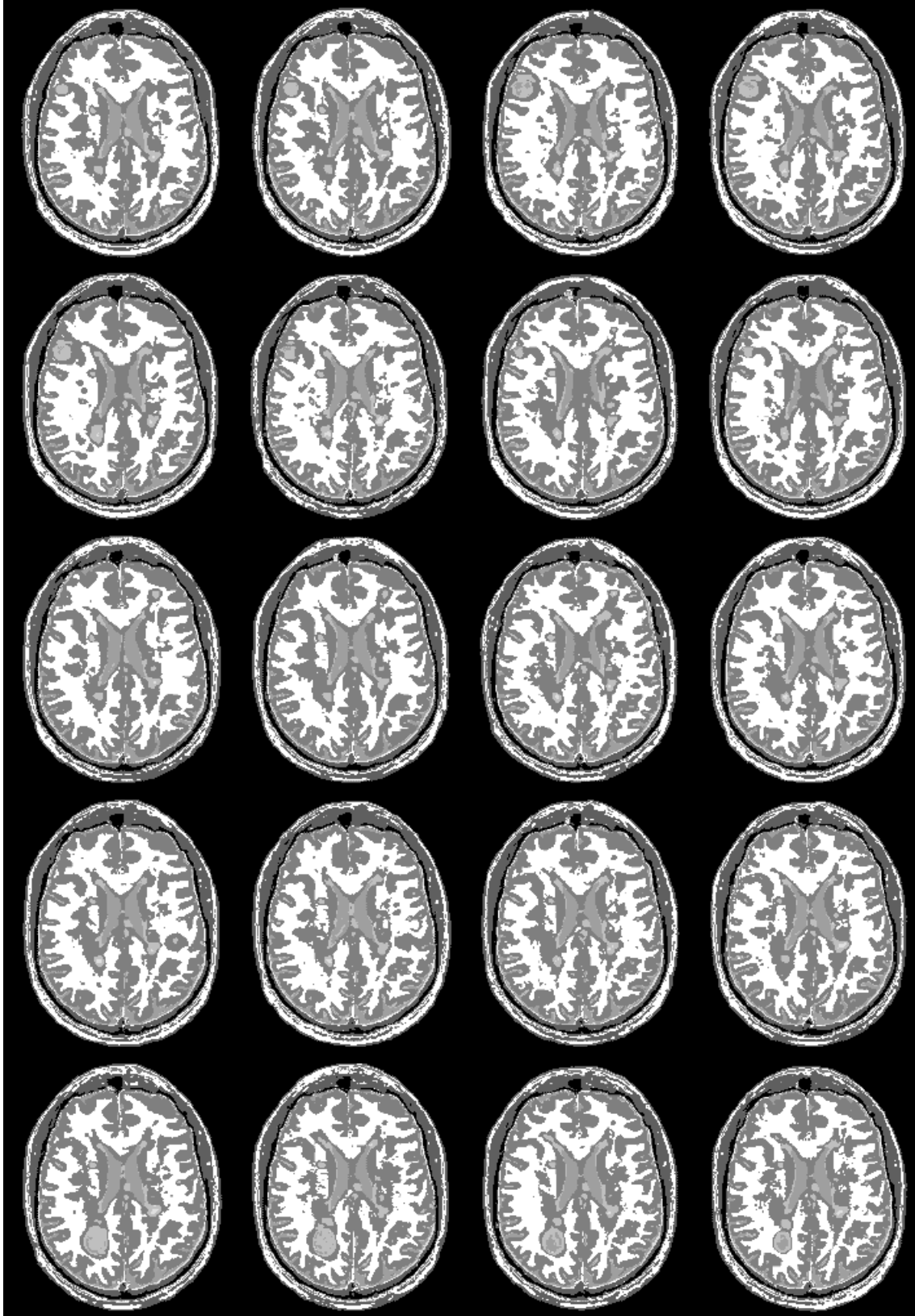


Figure 20: Adaptive segmentation results (without per-scan training)